Cell

Article

Shank3 oligomerization governs material properties of the postsynaptic density condensate and synaptic plasticity

Graphical abstract

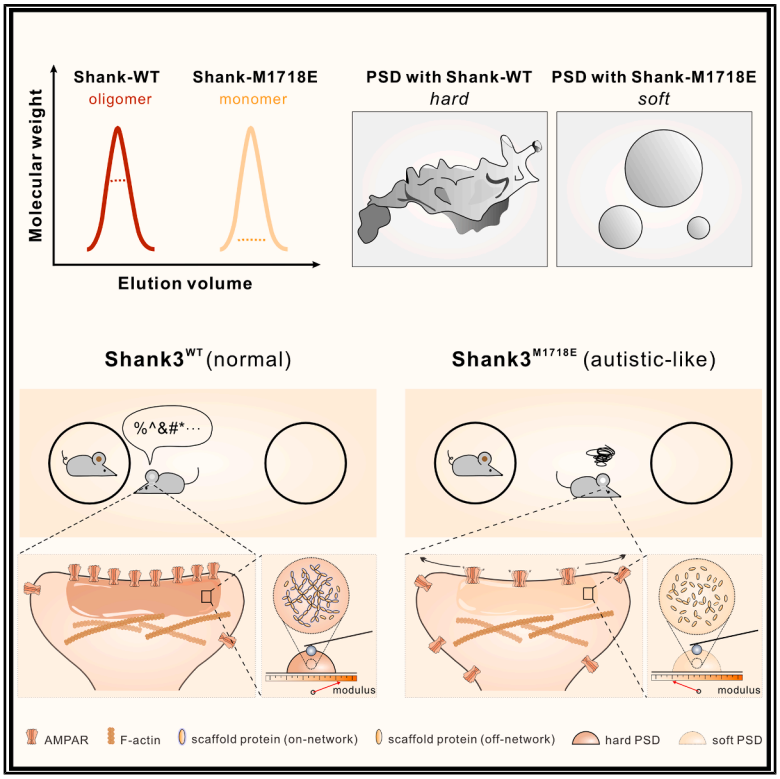

Highlights

- Shank3 oligomerization renders PSD condensate with soft glass-like material property
- Protein network property determines the PSD condensate material property
- Loss of Shank3 oligomerization softens PSD and impairs synaptic plasticity
- Material properties are critical to the functions of biological condensates

Authors

Bowen Jia, Zeyu Shen, Shihan Zhu, ..., Penger Tong, Wucheng Tao, Mingjie Zhang

Correspondence

zhangmj@sustech.edu.cn

In brief

The postsynaptic density (PSD) condensates in neuronal synapses are soft glass-like structures due to the formation of highly percolated protein-protein interaction networks. Shank3 oligomerization is critical for the soft glass-like PSD condensate formation. Defects in Shank3 oligomerization soften PSD, impair synaptic transmissions, and cause autism-like phenotypes in mice.

Jia et al., 2025, Cell *188*, 1–19
November 13, 2025
https://doi.org/10.1016/j.cell.2025.07.047

CellPress

Please cite this article in press as: Jia et al., Shank3 oligomerization governs material properties of the postsynaptic density condensate and synaptic plasticity, Cell (2025), https://doi.org/10.1016/j.cell.2025.07.047

Cell

CellPress

Article

Shank3 oligomerization governs material properties of the postsynaptic density condensate and synaptic plasticity

Bowen Jia,[1,2,7] Zeyu Shen,[1,2,7] Shihan Zhu,[1,2] Jingguo Huang,[3] Zhitao Liao,[4] Shuaizhu Zhao,[5,6] Hao Li,[5,6] Shiwen Chen,[1,2] Yang Xu,[1,2] Yu Wang,[1,2] Haitang Peng,[1] Guanhua Bai,[1] Youming Lu,[5,6] Penger Tong,[4] Wucheng Tao,[3] and Mingjie Zhang[1,8,*]

[1]School of Life Sciences, Southern University of Science and Technology, Shenzhen, China
[2]Division of Life Science, Hong Kong University of Science and Technology, Clear Water Bay, Kowloon, Hong Kong, China
[3]Fujian Key Laboratory of Translational Research in Cancer and Neurodegenerative Diseases, School of Basic Medical Sciences, Fujian Medical University, Fuzhou, China
[4]Department of Physics, Hong Kong University of Science and Technology, Clear Water Bay, Kowloon, Hong Kong, China
[5]Department of Pathophysiology, School of Basic Medicine and Tongji Medical College, Huazhong University of Science and Technology, Wuhan, China
[6]The Institute for Brain Research, Collaborative Innovation Center for Brain Science, Huazhong University of Science and Technology, Wuhan, China
[7]These authors contributed equally
[8]Lead contact
*Correspondence: zhangmj@sustech.edu.cn
https://doi.org/10.1016/j.cell.2025.07.047

SUMMARY

Cells contain numerous types of membraneless organelles or biological condensates formed via phase separation. Cellular biological condensates have broad material properties ranging from Newtonian fluids to elastic solids. How the material property of a biological condensate is regulated for cellular functions is poorly understood. Here, we discovered that, like native postsynaptic densities (PSDs), the reconstituted PSD condensate forms a soft glass material without signs of irreversible amyloid structure formation. Such glass-like PSD condensate formation is based on percolation of the PSD protein network via specific and multivalent interactions among scaffold proteins. Disruption of Shank3 SAM domain-mediated oligomerization, one type of *SHANK3* mutation observed in Phelan-McDermid syndrome patients, softened the PSD condensate by weakening its network percolation, impaired synaptic transmission and plasticity, and caused autistic-like behavior in mice. Thus, our study suggests that the material properties of the PSD condensate are critical for learning and memory mediated by neuronal synapses.

INTRODUCTION

Biological condensates or membraneless organelles are soft matters existing in cellular milieu and display a wide range of material properties. Living organisms harness a class of very stable biological condensates with soft glass-like material properties for physiological functions such as female germline specification,[1,2] embryo development,[3,4] neuronal synapse-mediated learning and memory,[5–7] immune responses,[8,9] cell growth, and tissue homeostasis.[10] Though very stable, these functional biological condensates can be dispersed or modified in response to signaling cues. Irreversible cellular condensates/aggregates are also prevalent and inescapably linked to pathophysiological conditions. Infamous cases of irreversible condensates are those found in neurodegenerative diseases such as aggregates containing TDP-43, Tau, α-synuclein, FUS, etc.[11–24] These irreversible condensates contain solid amyloid structures formed by stacking of cross-β motifs into long filaments with different shapes.[25]

Molecular mechanisms governing the formation and regulation of stable and functional/reversible condensates are much less understood. Limited evidence suggests that formation of amyloid-like structures is one mechanism for assembling this class of condensates. For example, formation of amyloid-like structure is driven by prion-like sequences of Xvelo for the Balbiani body in oocytes.[1] Reversible but gel-like FUS condensate is formed by a short peptide sequence in an intrinsically disordered region via cross-β stacking.[26] The low-complexity domain of ribonucleoprotein hnRNPA2 assembles as stable but reversible hydrogels via amyloid-like cross-β fibers.[27,28] Since the mechanism underlying biological condensate formation is multivalent interaction-mediated molecular network formation, we

Please cite this article in press as: Jia et al., Shank3 oligomerization governs material properties of the postsynaptic density condensate and synaptic plasticity, Cell (2025), https://doi.org/10.1016/j.cell.2025.07.047

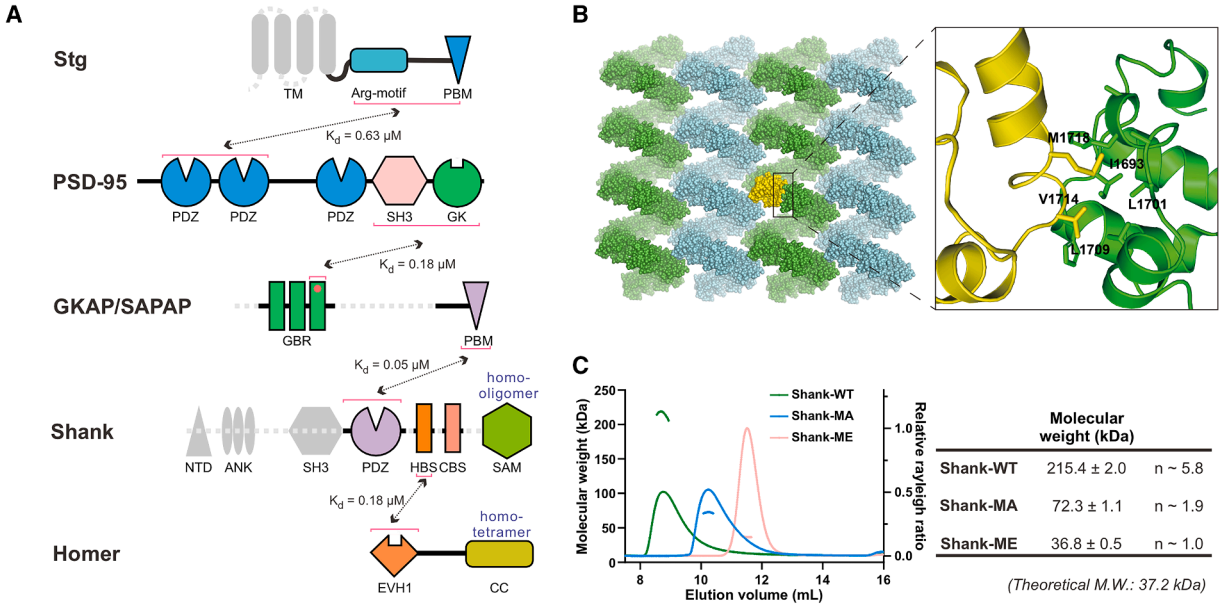

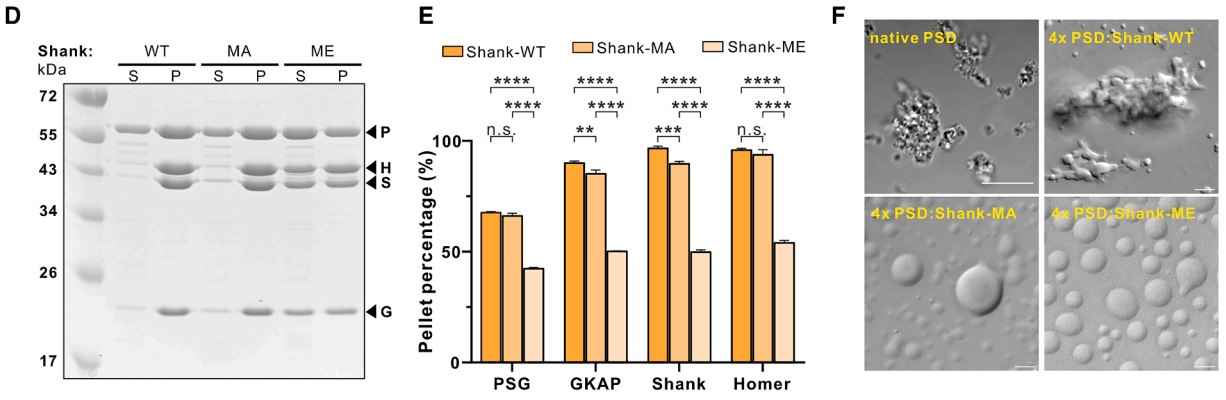

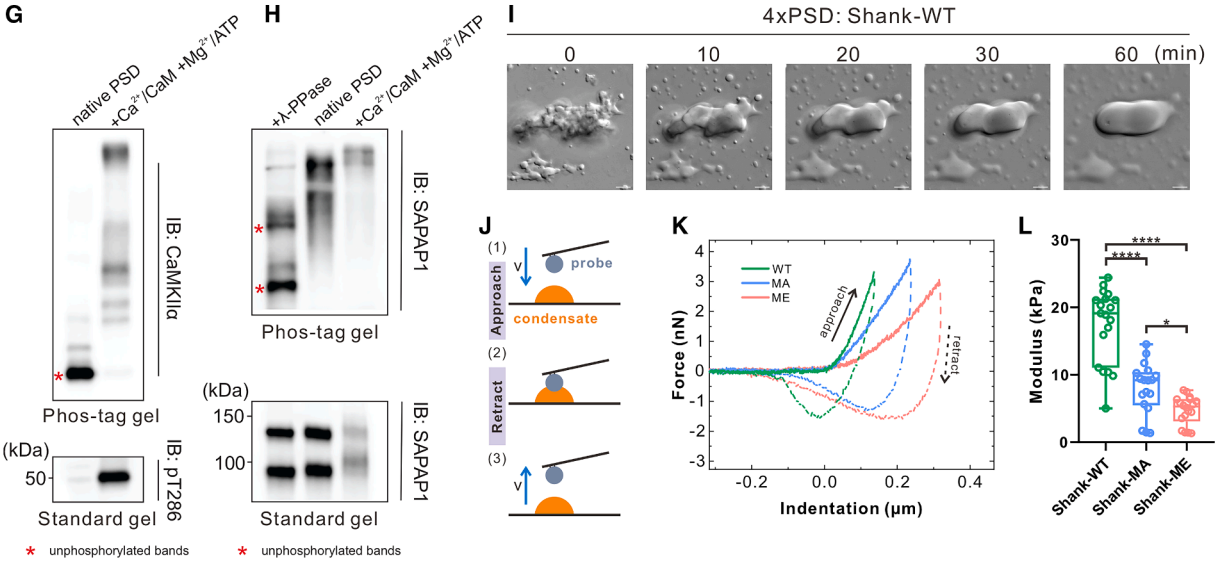

(legend on next page)

Please cite this article in press as: Jia et al., Shank3 oligomerization governs material properties of the postsynaptic density condensate and synaptic plasticity, Cell (2025), https://doi.org/10.1016/j.cell.2025.07.047

predict that highly stable soft glass-like condensates can form by increasing the valency and/or binding affinities of interaction nodes within the condensate molecular network.[29,30] Indeed, synthetic condensates with high stabilities have been demonstrated by either increasing network valency[31] or by engineering high-affinity node interactions.[32,33]

The postsynaptic density (PSD) of neuronal synapses is a specialized cellular structure essential for synaptic transmission, memory formation, and storage. Under electron microscopy (EM), PSDs are electron-dense (i.e., containing high concentrations of proteins) submicron-sized molecular assemblies with aspherical morphologies.[7,34] The PSD area is nearly linearly correlated with the activity of a synapse.[35,36] Stable PSDs in our brains can last for decades, and such long-lasting PSDs are thought to be essential for long-term memory storage. At the same time, PSDs can be rapidly modulated by synaptic stimulations.[37–41] Dynamic regulations of PSDs are critical for synaptic plasticity.[42,43] Biochemically purified PSDs are gel- or soft glass-like stable structures resistant to harsh detergent extractions.[44,45] PSDs are assembled by an array of multi-domain scaffold proteins, including PSD-95, SAPAP, Shank, and Homer. These scaffold proteins interact with each other specifically and with high affinities, forming PSD condensates with intricate and percolated molecular networks capable of clustering neurotransmitter receptors and enriching signaling enzymes.[46–50] Numerous mutations have been identified in each of these scaffold proteins from patients suffering from broad spectrums of brain disorders. Mutations of *SHANK3* are particularly prevalent in patients suffering from neurodevelopmental disorders with clinical symptoms including intellectual disability, autism spectrum disorders, seizures, dysmorphic organ/tissue development, etc.[51–54]

In this study, we discovered that, analogous to the purified PSD from the mouse brain, the reconstituted PSD condensate forms highly stable but dynamically reversible structures with soft glass-like morphology. The material property of the PSD condensate is directly correlated with the percolation level of the molecular network formed by the PSD scaffold proteins. Converting the Shank3 SAM domain from an oligomer to a monomer weakened PSD network percolation, leading to softening of the PSD condensate, increasing of AMPAR mobility, impairments of synaptic transmission and plasticity, and autistic-like behavior in mice.

RESULTS

Reconstituted PSD forms soft glass-like condensate

The four scaffold proteins of the PSD (PSD-95, SAPAP or GKAP, Shank, and Homer) serve as the drivers for the PSD condensate formation.[46,47,55] Thus, we used reconstituted PSD condensates containing the four scaffold proteins (referred to as 4x PSD; Figure 1A) to investigate the PSD material properties. The Shank SAM domain can form sheet-like structures due to the SAM domain self-oligomerization,[56] and Met1718 (the mouse Shank3 numbering) is critical for the hydrophobic interaction-mediated oligomerization of Shank3 SAM indicated by the crystal structure of wild-type SAM (SAM_WT) solved here and the previously reported SAM_ME structure (Figure 1B; Table S1).[56] We substituted Met1718 with Ala (termed as Shank-MA) or with Glu (Shank-ME) to weaken the hydrophobic interaction between the SAM domains at different grades.[48,56] The M1718E mutation does not alter the overall structure of the SAM domain (Figure S1A). The Shank protein with Shank-WT exhibited strong and concentration-dependent oligomerization in solution. The Shank-MA SAM could still oligomerize but with a weaker capacity. The Shank-ME SAM became a clean monomer (Figures 1C and S1B). We tested the role of Shank oligomerization in the PSD condensate formation using the 4x PSD system. Note

Figure 1. Reconstituted PSD forms gel-like condensate with soft glass-like material properties

(A) Schematic diagram showing the components and domain organizations of the proteins for the reconstituted PSD system.[46,47,57] The parts shaded in gray were removed from the recombinant proteins. The phosphorylated GBR of GKAP is marked with a red circle.

(B) Crystal packing of WT Shank3 SAM domain structure showing the helical fiber-mediated sheet formation. Zoomed-in image illustrates that Met1718 is at the center of the hydrophobic interface between two interacting SAM domains.

(C) FPLC-coupled static light scattering showing the oligomerization states of Shank-WT, Shank-MA, and Shank-ME (100 μM loading concentration). The fitted molecular weights (mean ± SD) are listed in the table.

(D) Representative SDS-PAGE showing the fraction distributions of the four PSD proteins recovered in the dilute phase/supernatant (S) and in the condensed phase/pellet (P). The concentration was 10 μM for each component. For the protein band labeling, P, PSD-95_PDZ-SH3-GK (PSG) supramodule with a Trx tag; H, Homer; S, Shank; and G, GKAP.

(E) Quantification showing the pellet percentage from (D). Data were from 3 independent batches of experiments and presented as mean ± SD. One-way ANOVA followed by Tukey's post hoc test; n.s., not significant; $^{**}p < 0.01$, $^{***}p < 0.001$, and $^{****}p < 0.0001$.

(F) Representative DIC images of purified PSD and reconstituted 4x PSD condensates. Scale bar: 10 μm.

(G) Native PSD purified from mouse brains contained a basal level of CaMKIIα. CaMKIIα in native PSD was activated by Ca^{2+}/CaM and Mg^{2+}/ATP. The phosphorylation level of CaMKIIα was probed by shifting of CaMKIIα bands in the Phos-tag gel (top panel) or with anti-CaMKIIα-pT286 antibody (bottom panel).

(H) The phosphorylation level of SAPAP1 in native PSDs was probed by shifting of SAPAP1 bands in the Phos-tag gel (top panel) and standard SDS-PAGE probed by anti-SAPAP1 antibody (bottom panel). PSDs purified from mouse brains were incubated with 10 μM λ-phosphatase (λ-PPase) or Ca^{2+}/CaM and Mg^{2+}/ATP.

(I) Time-lapse images showing fusion and smoothening of Shank-WT-containing PSD condensates. Note that the image at the time point 0 is the same as the "4x PSD: Shank-WT" in (F). Scale bar, 10 μm.

(J) Schematic diagram of the 4x PSD mechanical property measurement by AFM.

(K) Representative force indentation curves measured on the 4x PSD condensates with the approach curves in solid lines and the retraction curves in dashed lines.

(L) The elastic modulus of the 4x PSD condensates extracted from the force indentation curves by fitting with the Hertz model. Data were collected from three independent batches of condensates and presented as min-to-max. The average modulus of condensates containing Shank-WT, Shank-MA, and Shank-ME is 17.4 kPa (n = 19 droplets), 8.0 kPa (n = 18), and 4.7 kPa (n = 18), respectively. One-way ANOVA followed by Tukey's post hoc test; $^{*}p < 0.05$, $^{****}p < 0.0001$.

Please cite this article in press as: Jia et al., Shank3 oligomerization governs material properties of the postsynaptic density condensate and synaptic plasticity, Cell (2025), https://doi.org/10.1016/j.cell.2025.07.047

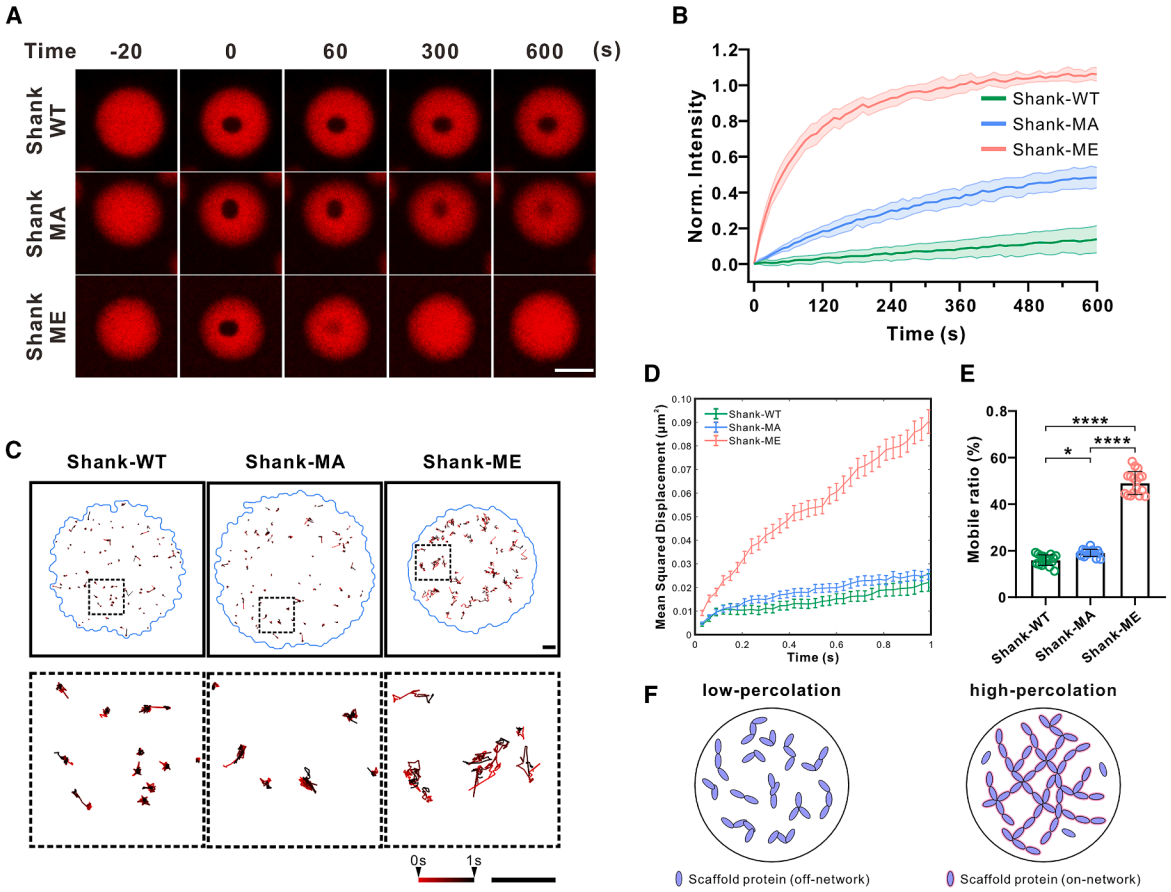

I

$$F(t)/F(0) = C_1 e^{-t/\tau_1} + C_2(1+t/\tau_2)^{-\alpha} + C_\infty$$

Group	C_1	C_2	C_∞	τ_1 (ms)	τ_2 (ms)	α
Shank-ME	0.86	0.13	0	1.8	4.8	0.23
Shank-MA	0.76	0.23	0	3.9	6.5	0.35
Shank-WT	0.57	0.30	0.13	4.3	57	0.77

(legend on next page)

Please cite this article in press as: Jia et al., Shank3 oligomerization governs material properties of the postsynaptic density condensate and synaptic plasticity, Cell (2025), https://doi.org/10.1016/j.cell.2025.07.047

that none of the protein-protein interactions except for the Shank3 self-oligomerization in the PSD network shown in Figure 1A were altered by the Shank3 SAM mutations. In a centrifugation-based phase separation assay, the 4x PSD condensates containing Shank-WT, -MA, or -ME displayed decreasing phase separation capacities (Figures 1D and 1E). Thus, the SAM domain-mediated Shank3 oligomerization plays a vital role in the PSD condensate formation.

Differential interference contrast (DIC) images revealed that the 4x PSD condensates containing Shank-ME or Shank-MA had spherical droplet morphology. By contrast, the 4x PSD condensate containing Shank-WT was amorphous and gel-like, similar to biochemically purified PSDs[44,45] (Figure 1F), indicating that the SAM domain of Shank contributes to the material properties of the PSD condensate. Time-lapse images captured slow rounding processes of the 4x PSD condensate containing Shank-WT from amorphous shapes to smooth and spherical droplet-like morphologies, indicating that the formed PSD condensate is still dynamic and with a soft glass-like structure (Figure 1I).

The gel-like reconstituted PSD condensate can be converted into droplets by adding an excess amount of Homer1a, the monomeric isoform of Homer1 and a well-known physiological negative regulator of the PSD (Figure S1C). In the purified native PSD from mice, CaMKIIα was found to be at a non-phosphorylated state with little phosphorylation on T286. Addition of Ca^{2+}/CaM converted essentially all CaMKIIα into phosphorylated states as probed by Phos-tag gel and by a pT286-specific antibody of CaMKIIα (Figure 1G). We also probed a key PSD scaffold protein, SAPAP1, in the purified PSD. SAPAP1 in the purified PSD is with mixed phosphorylation states. Treatment of the purified PSD with λ-phosphatase converted the majority of SAPAP1 into states with lower degrees of phosphorylation. Conversely, activating CaMKII by addition of Ca^{2+}/CaM converted SAPAP1 into states with more extensive phosphorylations (Figure 1H). These data indicate that PSDs, whether reconstituted *in vitro* or purified from the mouse brain, are reversible molecular assemblies that do not have obvious signs of irreversible amyloid-like structures.

Atomic force microscopy (AFM) was used to characterize the material properties of the 4x PSD condensate.[46,50] We conducted force indentation measurements by continuously compressing the 4x PSD condensates with the AFM probe at a fixed velocity (Figures 1J–1L). The measured force indentation curves revealed that the 4x PSD containing Shank-WT exerted more force than the condensates containing Shank-MA or Shank-ME at any given indentation (Figure 1K). The fitted values of elastic modulus from the curves showed that the PSD condensates containing Shank-WT had the highest elastic modulus, followed by the condensates containing Shank-MA and then the PSD condensates containing the Shank-ME (Figures 1L and S1D), suggesting more solid-like mechanical properties for Shank-WT-containing condensates compared with those with Shank-MA and Shank-ME.

Shank oligomerization controls the material properties of the PSD condensate

We next compared the dynamic properties of different forms of Shank in the 4x PSD condensate. Fluorescence recovery after photobleaching (FRAP) assay showed that the Shank-WT-containing condensate had the slowest recovery rate, followed by the Shank-MA condensate. By contrast, the Shank-ME-containing condensate showed rapid and near-full fluorescence signal recovery (Figures 2A and 2B), indicating that Shank oligomerization can dramatically slow down the overall dynamics of the 4x PSD condensates. We then used single-molecule tracking (SMT) to investigate the motion properties of individual molecules in the PSD condensate.[48] In the Shank-WT-containing condensate, each Shank molecule spent most of the time in the confined state but could switch to the mobile state for a small fraction of time (Figure 2C). Shank-MA in the condensate

Figure 2. The soft glass-like material properties of the PSD condensate are governed by the Shank SAM domain oligomerization

(A) Time-lapse images showing the fluorescence recovery of Shank molecules in the 4x PSD condensates after photobleaching. The concentration of each protein was 10 μM. Shank was labeled with Cy3 at a ratio of 1%. Scale bar, 5 μm.

(B) Quantification analysis of FRAP experiments. Data were collected from at least two batches of condensates for each variant and presented as mean ± SD. n = 10/9/12 droplets for Shank-WT/Shank-MA/Shank-ME, respectively.

(C) Representative images showing the single molecule motion trajectories of Shank proteins within the 4x PSD condensates with zoomed-in images shown in the bottom panels. Scale bar, 1 μm.

(D) Mean squared displacement (MSD) analysis of the Shank variants. Data were shown as mean ± SEM. The track numbers used for the analysis were 1,445/2,019/1,646 for Shank-WT/Shank-MA/Shank-ME.

(E) Quantification of mobile ratio (mean ± SD) of the Shank variants in the PSD condensates. The average mobile ratio of Shank-WT, Shank-MA, and Shank-ME is 16.0% (n = 17), 19.1% (n = 17), and 49.1% (n = 17). One-way ANOVA followed by Tukey's post hoc test; $^{*}p < 0.05$, $^{****}p < 0.0001$.

(F) Schematic diagram showing formation of percolated network within condensates. Left: condensate with a low-percolated protein network; right: a percolated protein network spanning the entire condensate.

(G) Schematic diagram showing the force-relaxation measurements for the 4x PSD condensates.

(H) Normalized force-relaxation curves for the 4x PSD condensates. Data are presented as mean ± SEM. n = 19/16/14 droplets for Shank-WT/Shank-MA/Shank-ME PSD condensates. The fitting to the relaxation curves was presented as dark-colored lines.

(I) The obtained relaxation parameters by fitting the relaxation curves with Equation (1) for the 4x PSD condensates.

(J) SDS-PAGE showing the fraction distributions of the PSD proteins in the dilute phase (S) and condensed phase (P) in the presence or absence of 10% 1,6-hexanediol. PSD proteins were composed of 5 μM Stg and 10 μM for the other four proteins.

(K) Quantification of pellet percentage (mean ± SD) of Shank proteins. Unpaired t test; $^{****}p < 0.0001$.

(L) SDS-PAGE showing the distribution of PSD proteins in the dilute phase (S) and the condensed phase (P) in the presence or absence of 200 μM Homer1a. The concentrations of the PSD proteins are the same as in (J).

(M) Quantification of pellet percentage (mean ± SD) of Shank proteins. Unpaired t test; $^{**}p < 0.01$, $^{***}p < 0.001$.

Data were collected from three independent batches of experiments unless specified otherwise.

Please cite this article in press as: Jia et al., Shank3 oligomerization governs material properties of the postsynaptic density condensate and synaptic plasticity, Cell (2025), https://doi.org/10.1016/j.cell.2025.07.047

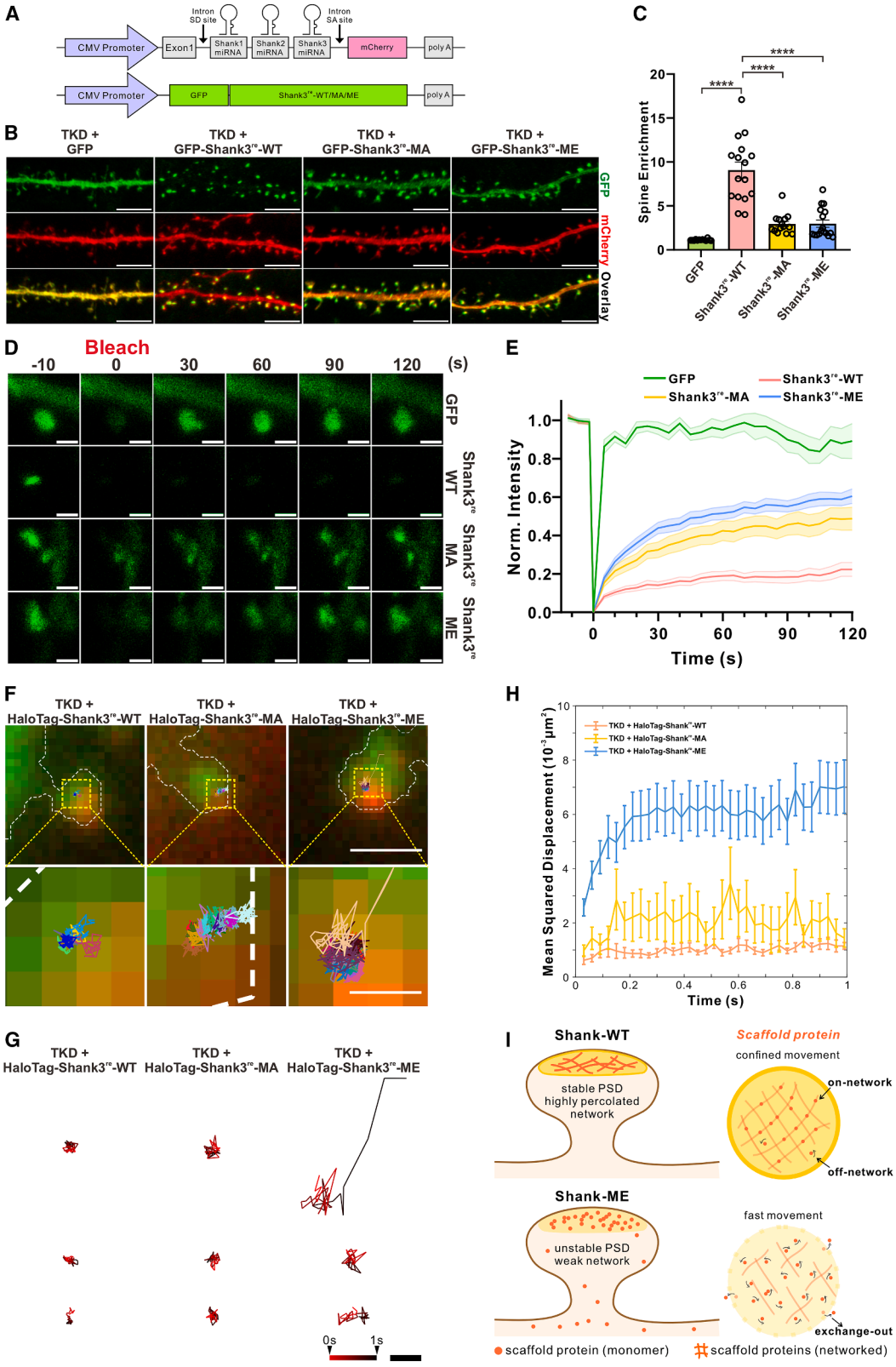

(legend on next page)

Please cite this article in press as: Jia et al., Shank3 oligomerization governs material properties of the postsynaptic density condensate and synaptic plasticity, Cell (2025), https://doi.org/10.1016/j.cell.2025.07.047

showed a higher mobility compared with Shank-WT. In sharp contrast, Shank-ME spent a much higher fraction of time in the mobile state and thus had a much larger diffusion coefficient in the condensate (Figures 2D, 2E, and S2D). The SMT results revealed that the PSD condensate containing Shank-WT formed a highly percolated network structure with most molecules bound onto the network, whereas the Shank-ME-containing condensate had a much lower level of percolation[48,50] (Figure 2F).

We next performed AFM-based force-relaxation measurements on the 4x PSD condensates to further probe their viscoelastic properties (Figure 2G). The force relaxation of the 4x PSD condensates follows an initial exponential decay and a long-time power-law decay (Figure 2H), which can be described by the equation:

$$\frac{F(t)}{F(0)} = C_1 e^{-\frac{t}{\tau_1}} + C_2\left(1+\frac{t}{\tau_2}\right)^{-\alpha} + C_\infty, \qquad \text{(Equation 1)}$$

where C_1, C_2, and C_∞ are the weighting factors for the exponential decay, power-law decay, and the persistent constant that does not vanish at long times; τ_1 and τ_2 are the characteristic times for the exponential decay and power-law decay; and α is the power-law exponent. The two relaxation modes, the exponential relaxation and power-law relaxation, are distinctive features of the viscoelastic properties of the PSD condensates.[50] The exponential relaxation comes from the molecular diffusion in the condensates, while the power-law relaxation is attributed to the structural rearrangement of the percolated molecular network inside the condensates. The observed power-law rheology of the PSD condensate is a hallmark of a disordered percolated network with a broad range of relaxation times for structural rearrangements, which is an important feature of soft glassy materials.[50,58–61] The six relaxation parameters provide a quantitative description of the material properties of the condensates (Figure 2I).

We found that (1) with the increase of Shank oligomerization, the degree of molecular network percolation of the 4x PSD condensates also increases evidenced by decrease of the diffusive component C_1 and concomitant increase of the network component C_2; (2) the exponential relaxation time τ_1 increases from 1.8 to 4.3 ms for the 4x PSD condensate with Shank-WT compared with that with Shank-ME, indicative of a less diffusive behavior in the condensates, which is consistent with the FRAP experiment in Figure 2B; and (3) the power-law relaxation time τ_2 also becomes longer for Shank-WT-containing 4x PSD condensate (57 ms for WT versus 4.8 ms for ME), revealing that the network dynamics is considerably lower and the protein molecules become more resistant to dissociation from the network for the Shank-WT-containing 4x PSD condensate. Interestingly, the 4x PSD condensate containing Shank-WT has a non-zero value of the persistent constant C_∞ that does not relax over a long time (C_∞ = 0.13). This unique constant implied that the network percolation in 4x PSD with Shank-WT is so strong that a nearly permanent (over the AFM experiment time frame of ~10 s) and elastic network has emerged. Notably, the motion properties of GKAP, Homer, and in particular PSD-95, which is not directly bound to Shank (Figure 1A), were also affected by alteration of Shank oligomerization (Figures S2A–S2C and S2E–S2H). The above material property characterizations reveal that the reconstituted PSD condensate is soft-glass like, where softness refers to its low values of Young's modulus and glassy nature refers to its power-law relaxation behavior.

A stably organized condensate should be more robust in resisting external perturbations. 1,6-hexanediol is widely used to dissolve hydrophobic interaction-mediated phase separation.[12,62] Shank-WT-containing PSD condensate could tolerate 10% 1,6-hexanediol, with only a small fraction of proteins dispersed to the supernatant fraction. Remarkably, Shank-ME-containing PSD condensate was totally dissolved by 10% 1,6-hexanediol (Figures 2J, 2K, and S3A–S3C). Homer1a is upregulated during sleep, accompanied by global downscaling of PSD sizes in synapses.[63–66] To mimic activity-dependent Homer1a expression, we added excess amounts of Homer1a to the reconstituted Shank-WT or Shank-ME PSD condensates. The amounts of PSD proteins in the Shank-WT condensate were only slightly decreased upon addition of Homer1a. By contrast, a significant amount of each PSD protein was dispersed from

Figure 3. Softening the PSD condensate increases the mobility and weakens synaptic enrichment of Shank3 in synapses

(A) Schematic diagram of pan-Shank knockdown and rescue constructs.[67,68]

(B) Representative images showing the spine localization of GFP, GFP-Shank3-WT, GFP-shank3-MA, and GFP-Shank3-ME. MCherry serves as a cell filler. Scale bar, 5 μm.

(C) Quantification of spine enrichment fold of GFP, GFP-Shank3-WT, GFP-shank3-MA, and GFP-Shank3-ME upon pan-Shank knockdown. Data are presented as mean ± SEM. n = 13/16/14/17 neurons for GFP/GFP-Shank3-WT/GFP-Shank3-MA/GFP-Shank3-ME/. One-way ANOVA followed by Tukey's post hoc test; ****$p < 0.0001$.

(D) Time-lapse images showing the fluorescence intensity recovery after photobleaching of GFP, GFP-Shank3-WT, GFP-shank3-MA, and GFP-Shank3-ME upon pan-Shank knockdown. Scale bar, 1 μm.

(E) FRAP curves showing the recovery after photobleaching of GFP, GFP-Shank3-WT, GFP-shank3-MA, and GFP-Shank3-ME upon pan-Shank knockdown. Data were presented as mean ± SEM. n = 17/27/22/31 spines from 9/10/12/13 neurons for GFP/GFP-Shank3-WT/GFP-Shank3-MA/GFP-Shank3-ME.

(F) Representative images showing the single molecule trajectories with longer than 1 s duration of HaloTaged Shank3 variants upon pan-Shank knockdown. Zoomed-in images are presented at the bottom panel. Scale bar, 1 μm (top), 200 nm (bottom).

(G) Three representative trajectories for 1 s duration of HaloTag-Shank3 variants. Scale bar: 100 nm.

(H) MSD analysis (mean ± SEM) of HaloTag-Shank3 variants upon pan-Shank knockdown. n = 507/839/1,044 trajectories from 10/10/12 neurons for HaloTag-Shank3-WT/HaloTag-Shank3-MA/HaloTag-Shank3-ME.

(I) Cartoon graph illustrating PSD organizations with a highly percolated network (top panel, Shank-WT neuron) or with a weak network (bottom panel, Shank-ME neuron). Right panels are aerial views of the left panels.

Data were collected from three independent batches of experiments.

Please cite this article in press as: Jia et al., Shank3 oligomerization governs material properties of the postsynaptic density condensate and synaptic plasticity, Cell (2025), https://doi.org/10.1016/j.cell.2025.07.047

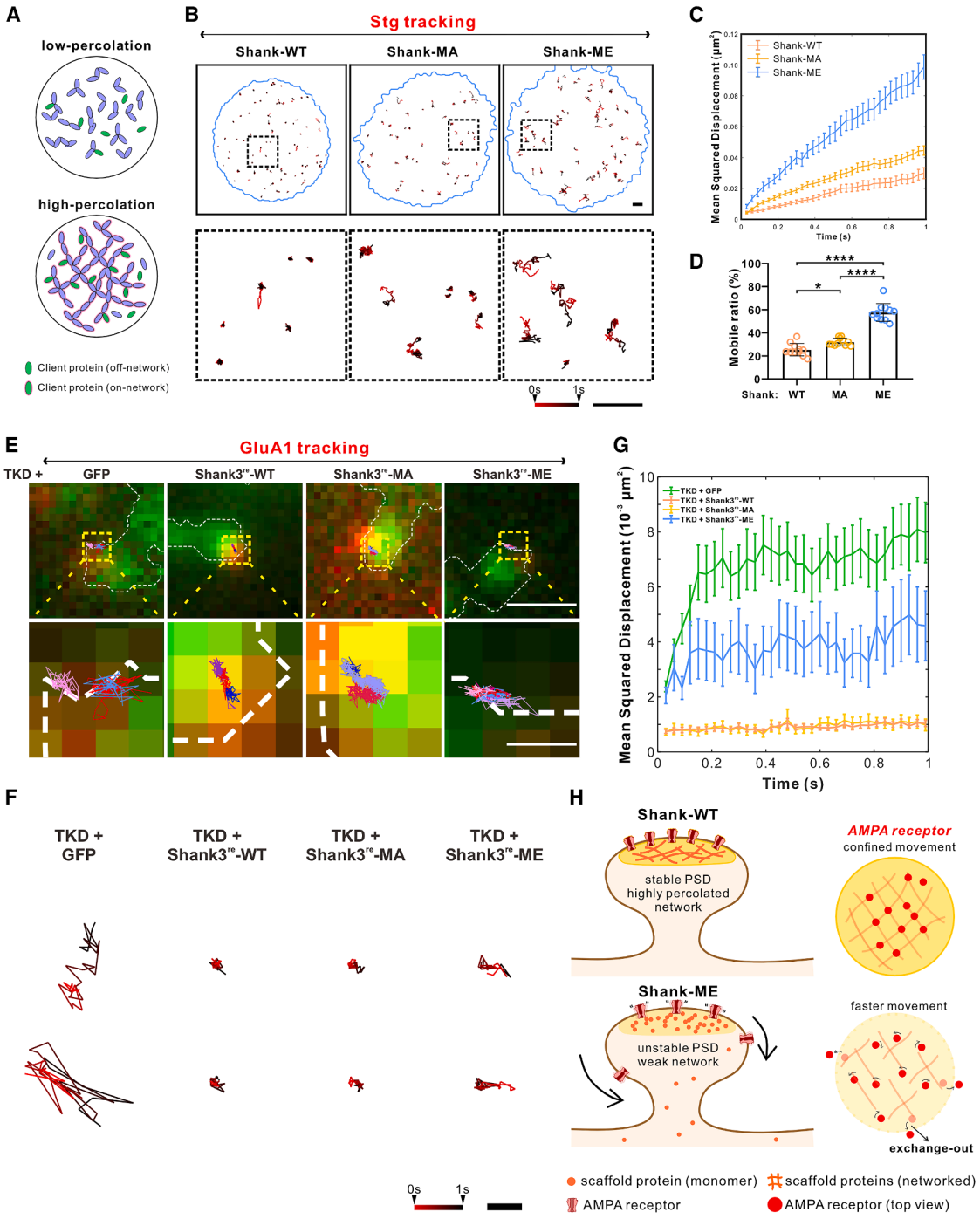

Figure 4. Softening the PSD condensate increases the mobility of AMPARs in synapses

(A) Schematic diagram showing the client proteins recruited into a condensate with a low- or high-percolated networks.

(B) Representative images showing the single molecule trajectories of Stg with a duration of 1 s within the 4x PSD condensates. Zoomed-in images are at the bottom of the corresponding panels. Scale bar, 1 μm.

(C) MSD analysis on Stg from condensates containing Shank-WT, Shank-MA, and Shank-ME. Data are presented as mean ± SEM. The track numbers used for the analysis were 2,896/3,115/2,326 for Shank-WT/Shank-MA/Shank-ME.

(D) Quantification of mobile ratio (mean ± SD) of Stg from condensates containing Shank-WT, Shank-MA, and Shank-ME. One-way ANOVA followed by Tukey's post hoc test; *$p < 0.05$, ****$p < 0.0001$.

(legend continued on next page)

Please cite this article in press as: Jia et al., Shank3 oligomerization governs material properties of the postsynaptic density condensate and synaptic plasticity, Cell (2025), https://doi.org/10.1016/j.cell.2025.07.047

the Shank-ME PSD condensate (Figures 2L, 2M, and S3D–S3F), further demonstrating that a softened PSD with Shank-ME is more susceptible to perturbations.

Shank oligomerization controls the dynamic properties of the PSD in living neurons

We next studied whether the SAM domain-mediated oligomerization of Shank is also critical for the percolated PSD network formation in living neurons. The Shank family consists of three *SHANK* genes (*SHANK1-3*), encoding three highly similar proteins. To avoid complications from possible compensations among the three isoforms, we applied a molecular replacement approach by knocking down all three isoforms of Shank (triple knockdown [TKD]) and concomitantly expressing one of the three Shank3 variants that are resistant to the RNA interferences (termed as Shank3^{re}) in cultured hippocampal neurons (Figure 3A).[67,68] Under such an experimental paradigm, we first investigated spine localizations of Shank3-WT, -MA, and -ME. GFP-tagged WT Shank3 (GFP-Shank3-WT) was highly enriched in dendritic spines (Figure 3B), consistent with a high partition coefficient *in vitro* (Figure S4). By contrast, the spine localizations of Shank3-ME and Shank3-MA were significantly compromised (Figures 3B and 3C). FRAP assay in living neurons showed the signals of the GFP tag rapidly recovered after photobleaching in dendritic spines, indicating that GFP molecules in dendritic spines and shafts were freely exchanging (Figures 3D and 3E). Signals corresponding to GFP-Shank3-WT showed little recovery, indicating stable organization of Shank3-WT in the PSD. By contrast, the GFP-Shank3-ME signals recovered much faster and to a higher level (to ~50%) compared with GFP-Shank3-WT (Figures 3D and 3E).

We further measured motion properties of Shank3-WT and the two mutants in synapses of living neurons by SMT. To achieve this, we knocked down all three isoforms of Shank and replaced them by expressing HaloTag-Shank3-WT or its mutants. Application of a tetramethylrhodamine (TMR)-HaloTag ligand afforded specific labeling of expressed Shank3 for SMT experiments. Figures 3F and 3G show example trajectories of HaloTag-Shank3 proteins acquired by the SMT experiments. MSD analysis of trajectories revealed that Shank3-WT molecules in synapses were largely confined within tiny areas with dozens of nanometers in diameter and a small apparent diffusion coefficient within the PSD. Shank3-ME, on the other hand, explored a significantly larger area and exhibited a larger apparent diffusion coefficient (Figures 3F–3H). The above imaging data from living neurons reveal that the PSD protein assembly is stable due to the formation of a highly percolated molecular network (Figure 3I, top). The PSD condensate molecular network can be destabilized by disrupting the SAM domain-mediated oligomerization of Shank (Figure 3I, bottom).

Material properties determine the dynamic properties of AMPARs

AMPAR diffusion plays critical roles in LTP and memory.[69,70] We next asked whether the network properties of the PSD condensate might also impact the dynamic property of AMPARs, which are at the edge and thus act as clients of the PSD network. In synapses, AMPARs are clustered and anchored to PSDs by binding to PSD-95 via its auxiliary TARP subunits such as Stargazin (Figure 1A).[47,71] To test whether AMPA receptor clustering into the PSD condensate relies on percolation of the PSD network, we included a low concentration (1 μM) of the cytosolic tail of Stargazin (Stg hereafter) into the reconstituted PSD condensate and measured its dynamics by SMT. Stg in the Shank-WT PSD condensate was locally confined within a small area for most of the time and could switch between the confined state and the mobile state (Figures 4A–4D). By contrast, Stg in the Shank-ME PSD condensate exhibited much faster dynamics and spent most of the time in the mobile state (Figures 4A–4D), consistent with the finding that the Shank-ME PSD condensate formed a much weaker network inside (Figures 2C–2E). The dynamics of Stg in the Shank3-MA condensate are between those of the Shank3-WT and Shank3-ME condensates.

We next measured the dynamics of AMPARs in synapses of living neurons by SMT using the same Shank replacement strategy. Endogenous AMPARs were labeled with an antibody recognizing the N-terminal domain of GluA1. Again, in synapses with all three Shank proteins replaced with Shank3-WT, GluA1 molecules were largely confined in a small area with sizes of a few dozen nanometers and with a small apparent diffusion constant, a finding that is consistent with previous observations.[72,73] If endogenous Shank proteins were replaced by a control GFP tag, GluA1 displayed rapid free motions, exploring much larger areas (Figures 4E–4G). In synapses with Shank proteins replaced by Shank3-ME, both the motion speed and areas of GluA1 exploration were significantly higher and larger compared with synapses containing Shank3-WT (Figures 4E–4G). These results revealed that the formation of the percolated PSD condensate network is critical for the nanoclustering and dynamic motions of AMPARs in synapses. Weakening the PSD network percolation weakened AMPAR clustering and increased the receptor mobility in synapses (Figure 4H).

(E) Representative images showing the single molecule trajectories of the endogenous GluA1 in synapses of neurons replacing Shank1-3 with GFP or GFP-Shank3 variants. Each color represents a single trajectory for longer than 1 s time duration. Zoomed-in images are presented at the corresponding bottom panel. Scale bar, 1 μm (top), 200 nm (bottom).
(F) Two representative GluA1 trajectories, each with a 1 s time duration, in synapses with GFP or GFP-Shank3 variants. Scale bar, 100 nm.
(G) MSD analysis (mean ± SEM) of endogenous GluA1 trajectories from neurons expressing GFP or GFP-Shank3 variants upon pan-Shank knockdown. n = 505/821/1,175/1,144 trajectories from 9/19/20/17 neurons expressing GFP/GFP-Shank3-WT/GFP-Shank3-MA/GFP-Shank3-ME.
(H) Cartoon graph illustrating AMPA receptor recruitment into the PSD with a highly percolated network (top panel, Shank-WT expressing neurons) or with a weak network (bottom panel, Shank-ME expressing neurons). Right panels are aerial views of the left panels.
Data were collected from three independent batches of experiments.

Please cite this article in press as: Jia et al., Shank3 oligomerization governs material properties of the postsynaptic density condensate and synaptic plasticity, Cell (2025), https://doi.org/10.1016/j.cell.2025.07.047

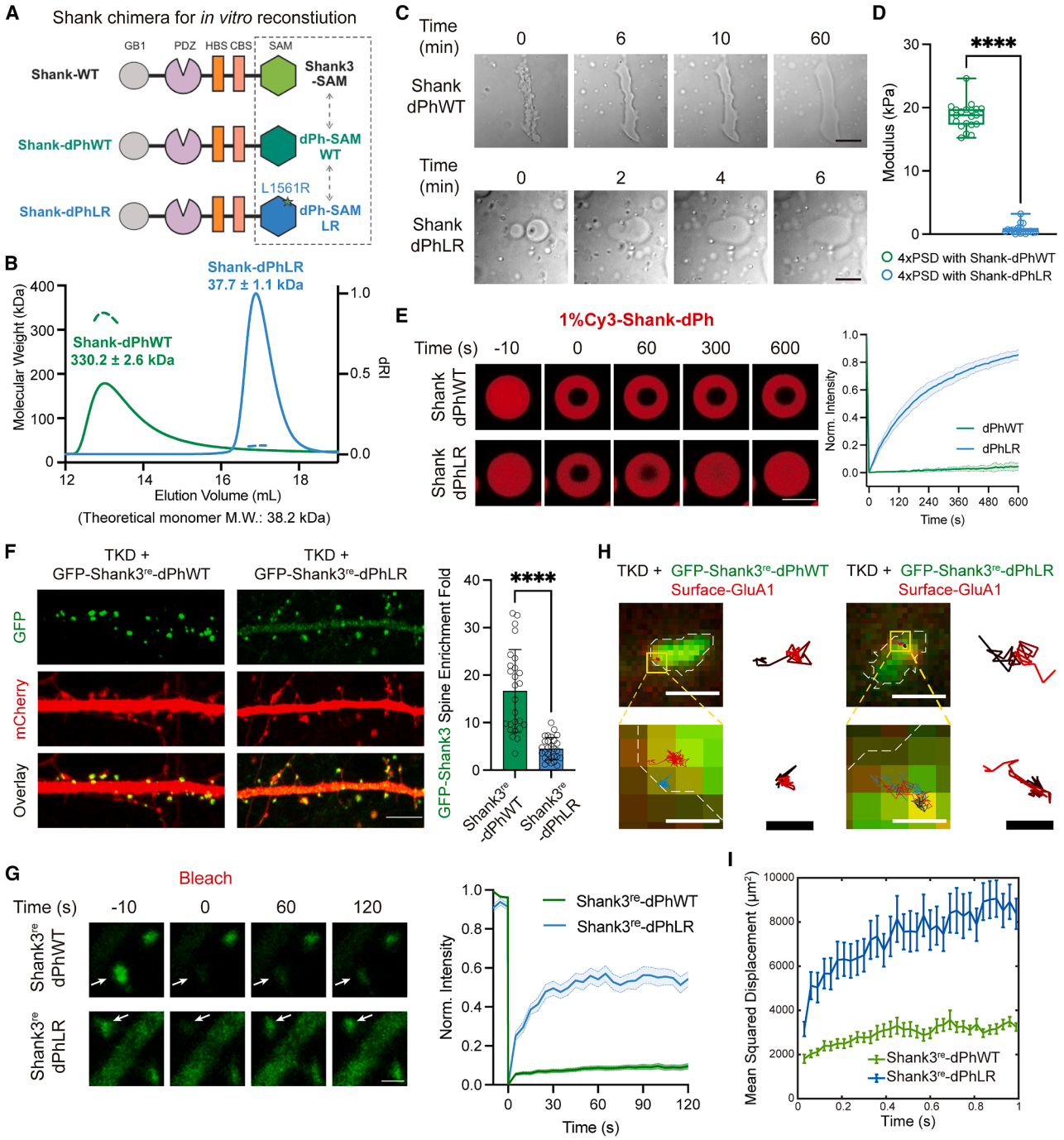

Figure 5. PSDs containing a Shank3 chimera with an orthogonal oligomerization domain have the same material and functional properties as the native PSDs

(A) Schematic diagram showing the design of Shank-dPhSAM chimeras used in biochemical and reconstitution assays.

(B) FPLC-coupled static light scattering showing the oligomerization states of Shank-dPhWT and Shank-dPhLR at the loading concentration of 100 μM. The fitted molecular weight marked above the peak is presented as mean ± SD.

(C) Time-lapse images showing fusion and smoothening of 4x PSD condensates containing Shank-dPhWT or Shank-dPhLR. The concentration was 20 μM for each component. Scale bar, 20 μm.

(D) The elastic modulus of the 4x PSD condensates extracted from the force indentation curves. Data were collected from two independent batches of condensate for each Shank variant and presented as min to max. The average modulus of condensates containing Shank-dPhWT and Shank-dPhLR are 18.7 kPa (n = 20 droplets) and 0.8 kPa (n = 18), respectively. Unpaired t test; ****p < 0.0001.

(legend continued on next page)

Please cite this article in press as: Jia et al., Shank3 oligomerization governs material properties of the postsynaptic density condensate and synaptic plasticity, Cell (2025), https://doi.org/10.1016/j.cell.2025.07.047

PSDs containing a Shank3 chimera with an orthogonal oligomerization domain have the same material and functional properties compared with the native PSDs

Although the SAM oligomer-to-monomer mutation is unique for probing roles of phase separation in the PSD protein assembly, it is formally possible that the SAM domain mutation might cause unexpected perturbations to the PSD protein interactions other than phase separation. To rule out such a possibility, we constructed a Shank3 chimera, in which the SAM domain is replaced by an orthogonal protein oligomerization domain with a similar size. We discovered that the SAM domain from Drosophila polyhomeotic (dPh for short) can act as an orthogonal oligomerization domain of Shank3 SAM (Figures 5A and S5). The SAM domain of dPh also oligomerizes into helical fibers (Figures S5A and S5B).[74] The reconstituted PSD condensates containing WT Shank-dPh behaved essentially the same as native Shank-WT in (1) enriching PSD proteins into the PSD condensates (Figure S5G), (2) forming gel-like PSD condensates with large elastic modulus (Figures 5C and 5D), and (3) causing low dynamics of scaffold proteins in the condensates (Figures 5E and S5H). Importantly, the monomeric Shank-dPh-L1561R (Shank-dPhLR) mutant mirrored the Shank3-M1718E mutant when comparing the above condensate properties (Figures 5B–5E, S5G, and S5H versus Figures 1 and 2). These *in vitro* data indicate that the SAM domain-mediated oligomerization of Shank and the Shank-dPh chimera determine the material properties of the reconstituted PSD condensates. Critically, when co-expressed in HeLa cells, the full-length Shank3-WT and Shank3-dPh chimeras formed demixed condensates (Figures S5C–S5F), indicating that Shank3-WT and Shank3-dPh are orthogonal.

Based on the above biochemistry data, we replaced the endogenous Shank1-3 with the Shank3-dPhWT chimera or its L1561R mutant (Shank3-dPhLR) in neurons using the same replacement strategy (Figure 3A). Shank3-dPhWT behaved very much like the WT Shank3 in having high synaptic enrichment (Figure 5F) and slow mobility in spines (Figure 5G). By contrast, the L1561R chimera, like the Shank3-M1718E mutant, showed weaker synaptic enrichment and higher mobility in spines. The GluA1 subunit of AMPAR in synapses containing the Shank3-dPhLR chimera also showed much higher mobility compared with spines containing the Shank3-dPhWT chimera (Figures 5H and 5I).

The data in Figure 5, together with results in Figures 1–4, reveal that the altered molecular mobility of PSD proteins, including AMPARs, and the resulting synaptic functional changes described below are driven by changes in the material properties of the PSD, caused by disrupted Shank3 oligomerization and a weakened percolated PSD network.

The soft glass-like PSD condensate is critical for AMPAR-mediated synaptic transmission

We next asked whether the glassy property of the PSD condensate is required for synaptic functions. We first assayed AMPA receptor synaptic transmission under the conditions of replacing all Shank proteins with different versions of Shank3 by biolistically transfecting neurons in organotypic hippocampal slices with corresponding DNA constructs (Figure 6A). AMPA receptor transmission was measured in the CA1 region around 1 week after transfection (Figure 6B). For neurons expressing GFP as the replacement, AMPAR currents decreased by >50%, compared with neighboring untransfected neurons (Figures 6C and 6F). Expression of WT Shank3 rescued the AMPAR currents back to ~75%, suggesting that Shank proteins are key scaffold proteins of PSD for AMPA receptor transmission (Figures 6D and 6F). The incomplete rescue is probably due to the expression level of exogenous Shank3 not being as high as the total amount of Shank1-3 proteins, as our replacement expression vector was driven by a medium-strength CMV promoter. The expression of Shank3-ME could hardly rescue AMPA receptor currents, revealing that the SAM domain-mediated oligomerization of Shank3 is essential for AMPA receptor synaptic transmission (Figures 6E and 6F).

We then investigated whether the formation of percolated PSD condensate plays a role in synaptic plasticity in mice using our Shank replacement strategy via viral infection-based delivery of various forms of Shank3 (Figure 6G1). Due to the packaging size limitation of AAV, we constructed a mini Shank3 gene (miniShank) by removing the disordered sequences of the protein and chaining functional domains/elements of Shank3 into a miniShank encoding gene with a size of ~1.9 kb (Figure 6G2). Two AAVs carrying Shank1/2/3 knockdown miRNA and miniShank were injected into neonatal mouse pups, and acute hippocampal slices were prepared at ~3 weeks after infection for long-term potentiation (LTP) measurements. In neurons where Shank1-3 were knocked down, LTP could not be induced (Figure 6H).

(E) Left panel: representative time-lapse images showing the fluorescence recovery of chimeric Shank in the 4x PSD condensates after photobleaching. The concentration of each protein was 10 μM. Shank was labeled with Cy3 at 1%. Scale bar, 5 μm. Right panel: quantification analysis of FRAP experiments. Data were from two batches of condensates for each variant and presented as mean ± SD. n = 10 droplets.

(F) Left panel: representative images showing the spine localization of GFP-Shank3^{re}-dPhWT and GFP-Shank3^{re}-dPhLR. MCherry serves as a cell filler. Scale bar, 5 μm. Right panel: quantification (mean ± SD) of spine enrichment fold of GFP-Shank3^{re}-dPhWT and GFP-Shank3^{re}-dPhLR upon pan-Shank knockdown. n = 26/28 neurons from two independent batches of cultures for GFP-Shank3^{re}-dPhWT/GFP-Shank3^{re}-dPhLR. Unpaired t test; ****$p < 0.0001$.

(G) Left panel: time-lapse images showing the fluorescence intensity recovery after photobleaching of GFP-Shank3^{re}-dPhWT and GFP-Shank3^{re}-dPhLR in living neurons upon pan-Shank knockdown. Scale bar: 1 μm. Right panel: FRAP curves of GFP-Shank3^{re}-dPhWT and GFP-Shank3^{re}-dPhLR. Data were presented as mean ± SEM. n = 32/26 spines from 16/14 neurons from three independent batches of cultures for GFP-Shank3^{re}-dPhWT/GFP-Shank3^{re}-dPhLR.

(H) Representative images showing the single molecule trajectories of the endogenous GluA1 in synapses of neurons replacing Shank1-3 with GFP-Shank3^{re}-dPhWT or GFP-Shank3^{re}-dPhLR. Each color represents a single trajectory for longer than 1 s time duration. Zoomed-in images are presented at the corresponding bottom panel. Scale bar, 1 μm (top) and 200 nm (bottom). In the right panel of each group, two representative GluA1 trajectories, each with a 1 s time duration, are displayed. Red, t = 0; black, t = 1 s. Scale bar, 100 nm.

(I) MSD analysis (mean ± SEM) of endogenous synaptic GluA1 trajectories from neurons expressing GFP-Shank3^{re}-dPhWT or GFP-Shank3^{re}-dPhLR upon pan-Shank knockdown. n = 862/627 trajectories from 19/24 neurons from three independent batches of cultures expressing GFP-Shank3^{re}-dPhWT/GFP-Shank3^{re}-dPhLR.

Please cite this article in press as: Jia et al., Shank3 oligomerization governs material properties of the postsynaptic density condensate and synaptic plasticity, Cell (2025), https://doi.org/10.1016/j.cell.2025.07.047

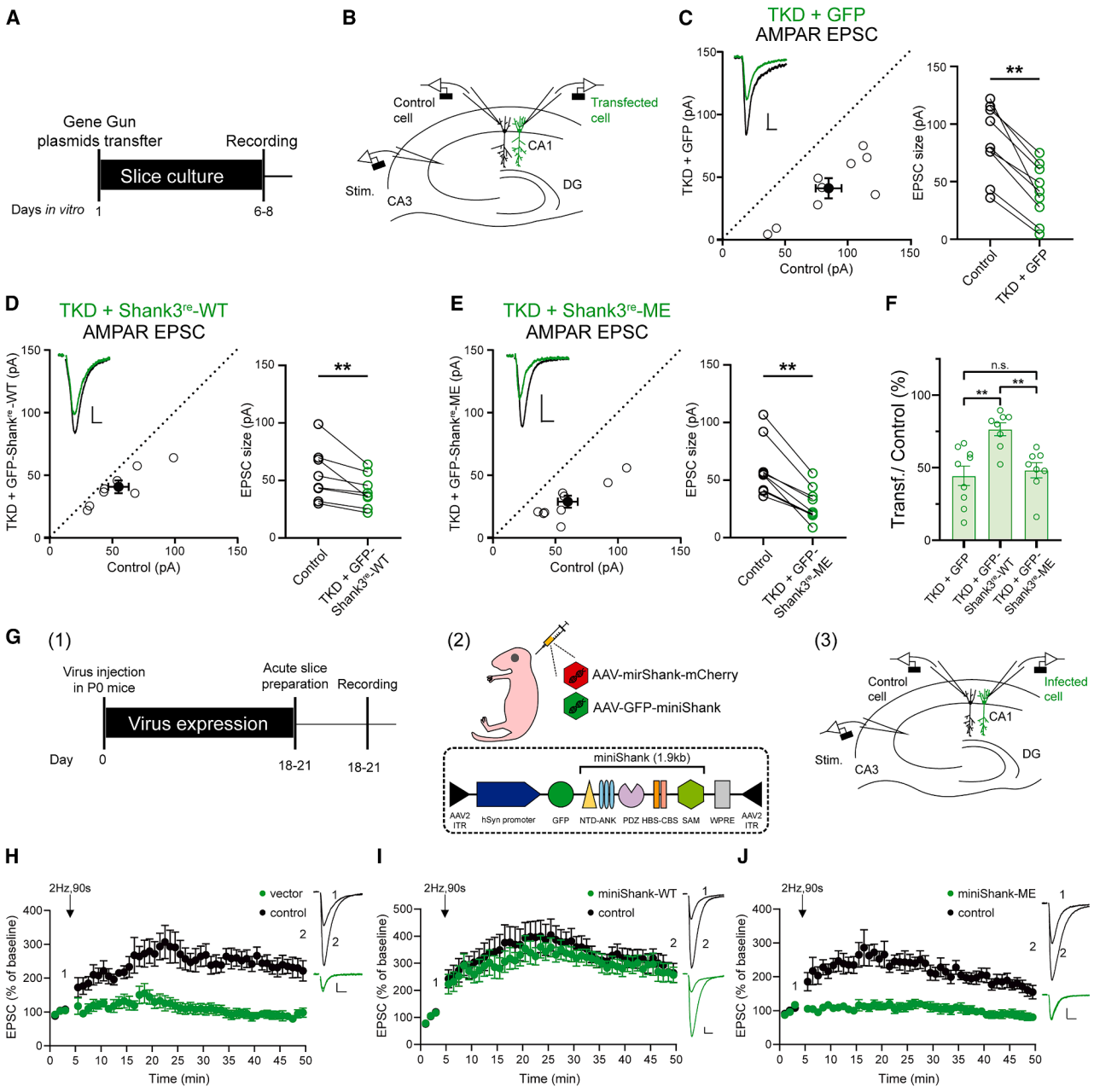

Figure 6. Softening the PSD condensate impairs basal synaptic transmission and LTP

(A) Schematic diagram of the timeline for the AMPA receptor basal transmission experiment.

(B) Scheme of simultaneous dual whole-cell recordings using rat hippocampal slice cultures. Pan-Shank knockdown construct was co-transfected with GFP or GFP-Shank3 variants.

(C-E) Scatterplots of AMPA receptor EPSC for single pairs (open circles) of the untransfected control and GFP (C, $n = 9$ pairs), GFP-Shank3-WT (D, $n = 8$), or GFP-Shank3-ME (E, $n = 9$) expressing cells. Filled circles represent mean ± SEM. Insets show sample current traces from the control (black) and transfected (green) neurons. Scale bars, 25 pA, 20 ms. Wilcoxon signed-rank test; $^{**}p < 0.01$.

(F) Bar graph showing the comparison of transfected versus control neuron AMPAR EPSC ratio in all conditions tested. One-way ANOVA followed by Tukey's post hoc test; ** $p < 0.01$.

(G) Scheme of LTP measurements. (1) Timeline of the LTP experiments. (2) Schematic diagram of gene delivery by virus infection in neonatal mice. Inset shows the construct expressing miniShank. (3) Scheme of simultaneous dual whole-cell recording in the LTP measurement.

(H–J) Plots showing AMPAR EPSC amplitude (mean ± SEM) in neurons replacing endogenous Shank1-3 with GFP (H, $n = 9$), GFP-miniShank-WT (I, $n = 10$), and GFP-miniShank-ME (J, $n = 10$). Insets show sample current traces before (1) and after (2) LTP induction from control (black) and infected (green) neurons. LTP induction is indicated with a black arrow. Scale bars, 25 pA, 20 ms.

Please cite this article in press as: Jia et al., Shank3 oligomerization governs material properties of the postsynaptic density condensate and synaptic plasticity, Cell (2025), https://doi.org/10.1016/j.cell.2025.07.047

CellPress

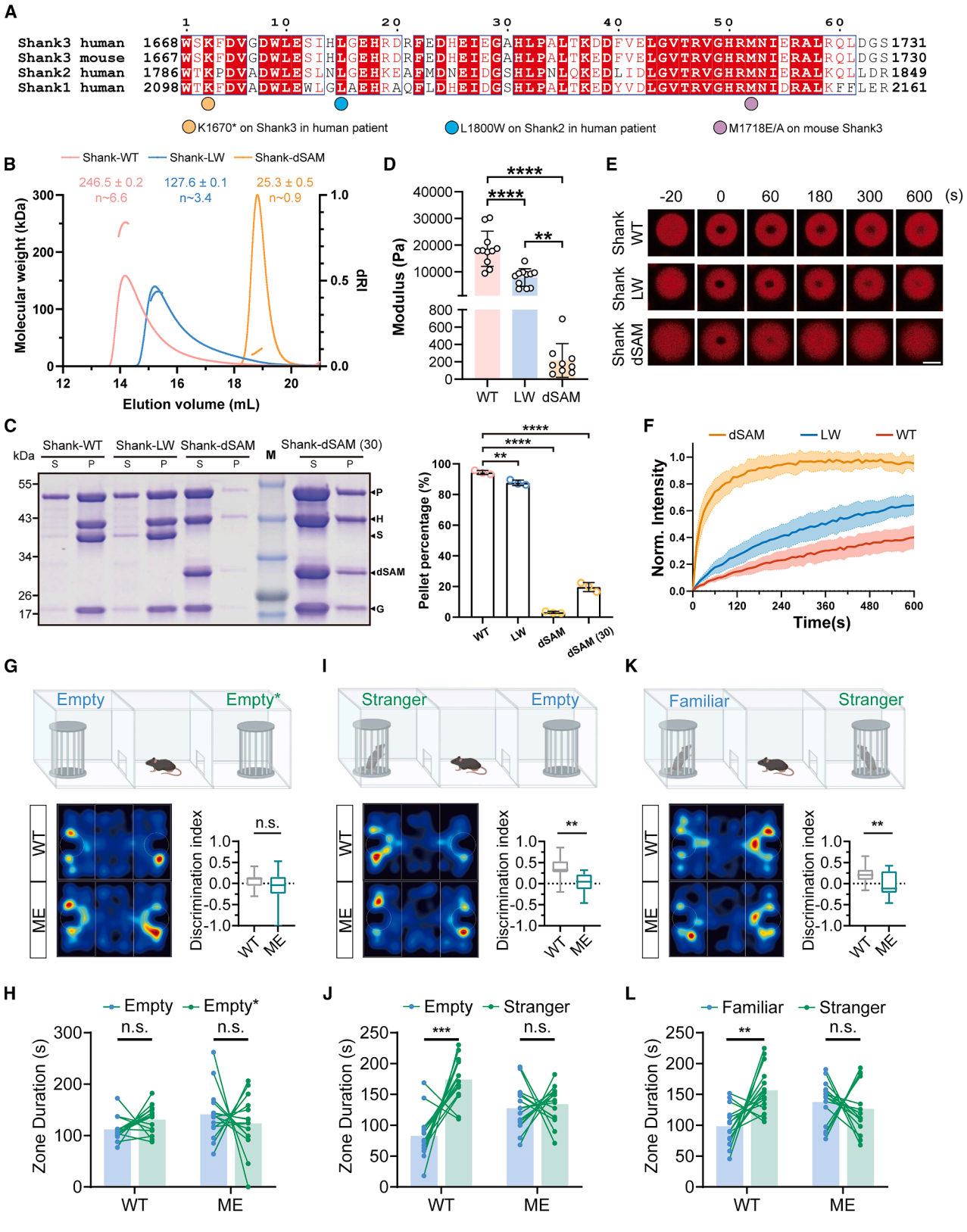

(legend on next page)

Please cite this article in press as: Jia et al., Shank3 oligomerization governs material properties of the postsynaptic density condensate and synaptic plasticity, Cell (2025), https://doi.org/10.1016/j.cell.2025.07.047

The pan-Shank knockdown-induced LTP deficit was rescued by expression of the WT miniShank, but not by miniShank-ME, indicating that Shank3 oligomerization-enhanced network percolation inside the PSD condensate is critical for LTP expression (Figures 6I and 6J).

Mutations of *SHANKs* with the SAM domain oligomerization defects cause brain disorders

Numerous disease-associated mutations have been identified in *SHANK2* and *SHANK3*.[53,54,75,76] Of particular interest, two patients were identified to have mutations in the SAM domain, and both patients exhibited intellectual disability and behavioral abnormalities. One is the L1800W mutation in Shank2,[76] and the other is K1670* in Shank3[53] (Figures 7A and S6A). We generated recombinant Shank proteins with the LW mutation (Shank-LW with Shank3 Leu1800 substituted with Trp) or with the SAM domain deletion (Shank-dSAM corresponding to K1670*) and found that oligomerization of Shank-LW was reduced when compared with Shank-WT, and Shank-dSAM totally lost its ability to oligomerize (Figure 7B). In a centrifugation-based phase separation assay, Shank-LW displayed similar phase separation capacity like Shank-WT did (with 10 μM of each protein), indicating that the bulk phase separation was not obviously affected by the mutation (Figure 7C). Whereas for the Shank-dSAM mutant, its phase separation threshold was increased to ∼30 μM (Figure 7C). AFM-based measurements showed that the elastic modulus of 4x PSD condensate containing Shank-LW is significantly lower than that of Shank-WT (Figure 7D). In a FRAP assay, the PSD-95 signal recovered faster in Shank-LW-containing condensate than in Shank-WT-containing condensate (Figures 7E and 7F). The Shank-dSAM-containing condensate becomes remarkably fluidized, with its molecules becoming highly diffusive and its elastic modulus dramatically reduced (Figures 7D–7F). Hence, these disease-causing mutations of Shank proteins with weakened or disrupted SAM oligomerization could directly alter the PSD condensate formation and material properties.

Mouse models lacking either Shank2 or Shank3 displayed autistic-like behaviors.[77,78] To further investigate the relationship between Shank oligomerization and brain disorders, we generated homozygous Shank3^{M1718E} mutant (ME) mice (Figures S6B and S6C). Given the prevalence of social and cognitive impairments in patients with autism spectrum disorders, we explored whether similar phenotypes might exist in Shank3^{M1718E} mice. The open field test showed no significant differences between WT and ME groups in total moving distance, average speed, or time spent in the peripheral or central areas of the arenas (Figures S6D and S6E), indicating that the mutation of *SHANK3* does not affect general locomotor activity. Then we used a three-chamber social interaction test to probe animals for their voluntary initiation of social interactions and their ability to discriminate social novelties. In the habituation phase, all groups of mice had no location preference for any chambers (Figures 7G and 7H). In the sociability preference test (phase 2), the test animal was left to explore and to initiate social contact with a stranger held inside a wired cage or with an identical but empty cage. Unlike WT mice that clearly preferred stranger mice, ME mice failed to exhibit such preference (Figures 7I and 7J). In the social novelty test (phase 3),

Figure 7. Softening the PSD condensates causes brain disorders in humans and in mice

(A) Sequence alignment showing the conservation of the Shank SAM domain.

(B) FPLC-coupled static light scattering showing the profiles of recombinant Shank-WT, -LW, and -dSAM at a loading concentration of 100 μM. The fitted molecular weights (mean ± SD) are indicated at the top of each peak.

(C) SDS-PAGE showing the distribution of the PSD proteins in the dilute (S) and condensed (P) phases in the 4x PSD mixtures. The concentration of each protein was 10 μM, except for the group of Shank-dSAM(30), in which each protein was at 30 μM. The bar graph shows the quantification of the Shank proteins in the pellet. Data were from three independent batches of assays and presented as mean ± SD. One-way ANOVA followed by Tukey's post hoc test; $^{**}p < 0.01$, $^{****}p < 0.0001$.

(D) The elastic modulus (mean ± SD) of the 4x PSD condensates extracted from the force indentation curves. The average modulus of condensates containing Shank-WT, Shank-LW, and Shank-dSAM is 18.6 kPa ($n = 11$ droplets), 7.8 kPa ($n = 11$), and 0.2 kPa ($n = 9$), respectively. One-way ANOVA followed by Tukey's post hoc test; $^{**}p < 0.01$, $^{****}p < 0.0001$.

(E) Representative time-lapse images showing the fluorescence recovery after photobleaching of PSD-95-PSG in the 4x PSD condensates containing Shank-WT, Shank-LW, or Shank-dSAM, respectively. Scale bar, 5 μm.

(F) Quantification of the FRAP experiments in (E). Data were collected from two independent batches of experiments and presented as mean ± SD. $n = 13/12/8$ droplets for Shank-WT/Shank-LW/Shank-dSAM.

(G) Schematic diagram of the empty-empty social preference test, where both compartments contained empty cages. Left: representative heatmaps showing the exploration patterns of WT and *Shank3*^{M1718E} homozygous (ME) groups during the three-box social interaction test in round 1. Right: the boxplot showing the discrimination index for the three-box social interaction test in round 1, comparing WT and ME groups. Data were presented as min-to-max ($n = 15$ mice; unpaired t test; n.s., not significant).

(H) Bar graphs showing the zone duration comparing WT and ME groups during the three-box social interaction test in round 1. $n = 15$ mice; paired t test; n.s., not significant.

(I) Schematic diagram of the stranger-empty social novelty test, comparing interaction with a novel stranger mouse versus an empty cage. Left: representative heatmaps showing the exploration patterns of WT and ME groups during the three-box social interaction test in round 2. Right: the boxplot showing the discrimination index for the three-box social interaction test in round 2 ($n = 15$ mice; unpaired t test; $^{**}p < 0.01$).

(J) Bar graphs showing the zone duration comparing WT and ME groups during the three-box social interaction test in round 2. $n = 15$ mice; paired t test; n.s., not significant; $^{***}p < 0.001$.

(K) Schematic diagram of the familiar-stranger test, comparing interaction with a familiar mouse versus a novel stranger mouse. Left: representative heatmaps showing the exploration patterns of WT and ME groups during the three-box social interaction test in round 3. Right: the boxplot showing the discrimination index for the three-box social interaction test in round 3 ($n = 15$ mice; unpaired t test; $^{**}p < 0.01$).

(L) Bar graphs showing the zone duration comparing WT and ME groups during the three-box social interaction test in round 3. $n = 15$ mice; paired t test; n.s., not significant; $^{**}p < 0.01$.

Please cite this article in press as: Jia et al., Shank3 oligomerization governs material properties of the postsynaptic density condensate and synaptic plasticity, Cell (2025), https://doi.org/10.1016/j.cell.2025.07.047

WT mice exhibited robust social memory, spending significantly more time in the zone containing the novel stranger mouse compared with the zone with the familiar mouse. By contrast, ME mice showed impaired social memory, as they spent similar amounts of time in the familiar and stranger zones (Figures 7K and 7L). As a control, a series of anxiety-related behavioral tests showed that the ME mice did not display anxiety-like behavioral phenotypes (Figure S7).

Taken together, the biochemical, soft-matter physics, cell biological, and mouse model studies above collectively indicated that the formation of soft glass-like PSDs supported by a highly percolated PSD protein network is vitally important for synaptic and brain functions.

DISCUSSION

LTP is widely accepted as the cellular mechanism for learning and memory in the animal brains. Molecularly, LTP generation by synaptic stimulations causes accumulation and clustering of AMPARs at excitatory synapses so that these synapses become stronger. To maintain LTP, these newly added AMPARs need to be stably anchored to the PSD.[79] In this study, we discovered that the stability of AMPARs in synapses, measured by the clustering density and mobility of the receptors, is intimately regulated by the material properties of the PSD condensate. We found that PSDs purified from native synapses or reconstituted *in vitro* are glassy structures without obvious amyloid-like assembly, the material property of the PSD condensate is closely connected with the percolation level of the PSD protein network, and the Shank3 SAM domain-mediated oligomerization specifically determines the material property of the PSD condensate.

The abundance of scaffold proteins such as PSD-95 are believed to be critical in determining how many and how dense neurotransmitter receptors such as AMPARs can be accommodated in each synapse, and thus determining synaptic strength. During LTP, it is also believed that more PSD-95-like slot proteins are accumulated in PSD so that more receptors can be anchored to the synapse.[80] Our study suggests that such a slot theory needs to be revised. First, the entire PSD network collectively behaves as receptor binding slots, even though these receptors may only bind to one of these scaffold proteins. Second, the slots for receptors are dynamic. For example, the PSD network can be enhanced by CaMKII-mediated phosphorylation of SAPAPs and enhanced binding between phosphor-SAPAP and PSD-95 without adding new scaffold proteins.[57] Third, in addition to directly altering the interaction between receptors and their direct binding scaffold proteins, such as by Arc,[81] the receptor clustering in synapses can also be regulated by modulating the interactions between scaffold proteins in the network that are away from the direct binding site(s) (e.g., by Homer1a as shown in Figure 2L). Accordingly, mutations of genes encoding different synaptic proteins on the PSD molecular network can converge on overlapping neuronal disorders collectively referred to as synaptopathy.

From the perspective of condensate biology in general, the PSD condensate is not a conventional liquid-like condensate. Instead, it forms a soft-glass-like assembly with distinct material properties. Though soft-glass like, the PSD condensate is still dynamic and not amyloid-like. Thus, the PSD condensate may be viewed as a functional glassy protein assemblage. We anticipate that other non-amyloid-like functional glassy protein assemblages exist in living organisms. The material properties of functional glassy protein assemblages may be connected to many fascinating biological observations, such as the long-term viability of plant seeds, decades-long memory maintenance in the human brain, extreme protein longevity in mammalian oocytes, etc. It is remarkable that the PSD material property and its biological function are dramatically altered by one single amino acid residue change among the entire PSD network. This is an emergent property for biological condensates. We anticipate that such small perturbation-induced large material property changes on biological condensates may be harnessed for cellular functions such as acute and specific responses to stimulations in immune systems, sensitive sensing of cells to subtle environmental changes such as temperature or nutrient levels, responses of the nervous systems to various stimulations, etc.

Limitations of the study

There are several limitations of this study. First, we applied a panel of complementary techniques, including fluorescent microscopy, AFM measurements, and SMT, to investigate material properties of the PSD condensate reconstituted *in vitro*. Due to the tiny sizes of the native PSD in living neurons, we could not directly measure material properties under the native conditions. Second, although SMT experiments *in vitro* and in living neurons as well as AFM-based force-relaxation assays provide strong evidence supporting the existence of procolated molecular networks in the PSD condensate, direct visualization of such molecular networks has not been achieved for the PSD condensate or for other biological condensates to date. Cryo-electron tomography holds great promise in this direction.

RESOURCE AVAILABILITY

Lead contact

Further information and requests for resources and reagents should be directed to and will be fulfilled by the lead contact, Mingjie Zhang (zhangmj@sustech.edu.cn).

Materials availability

The Shank3M1718E mouse model is available through the lead contact and with a material transfer agreement.

Data and code availability

- The atomic coordinates of the Shank3-SAM domain are accessible via the Protein Data Bank under the accession number PDB: 9KSQ.
- Any additional information required to reanalyze the data reported in this work paper is available from the lead contact upon request.
- Original data are available on Mendeley Data (http://doi.org/10.17632/fr8zff4ncd.1).

ACKNOWLEDGMENTS

This work was supported by grants from the National Natural Science Foundation of China (82188101 to M.Z. and 32494762 to Z.S. and G.B.), the Shenzhen Talent Program (KQTD20210811090115021), the Shenzhen Science and Technology Basic Research Program (JCYJ20220818100215033), the Guangdong Innovative and Entrepreneurial Research Team Program (2021ZT09Y104), the Shenzhen Medical Research Fund (B2302039), and the Key-Area Research

and Development Program of Guangdong Province (2023B0303010001) to M. Z., National Natural Science Foundation of China (31721002, 81920208014, and 31930051 to Y.L., 32200795 to H.L., and 82471436 to W.T.), and the Natural Science Foundation of Hubei Province, China (2022CFB608 to H.L.). We thank Dr. Harold MacGillavry for the Shank knockdown and rescue constructs, the BL19U1 beamline at the National Facility for Protein Science Shanghai for X-Ray beam time, and the Biosciences Central Research Facility at HKUST for providing super-resolution imaging microscopy.

AUTHOR CONTRIBUTIONS

B.J. and M.Z. conceived the idea and designed the experiments; B.J. and S. Zhu performed all biochemical experiments and cell biology experiments with help from S.C., Y.X., Y.W., H.P., and G.B.; Z.S. and B.J. performed SMT experiments; Z.L. performed AFM experiments; J.H. performed electrophysiology experiments; H.L. and S. Zhao performed mouse behavior experiments; and all authors analyzed the results. B.J., Z.S., S. Zhu, and M.Z. wrote the manuscript with input from other authors. P.T., Y.L., W.T., and M.Z. supervised the research. M.Z. coordinated the project.

DECLARATION OF INTERESTS

The authors declare no competing interests.

STAR★METHODS

Detailed methods are provided in the online version of this paper and include the following:

- KEY RESOURCES TABLE
- EXPERIMENTAL MODEL AND STUDY PARTICIPANT DETAILS
  - Animals
  - Primary hippocampal neuron culture
- METHOD DETAILS
  - DNA constructs
  - Protein expression and purification
  - Protein crystallography and structure determination
  - Protein fluorescence labeling
  - Size-exclusion chromatography coupled with multi-angle light scattering assay
  - Phase separation sedimentation and imaging assay
  - Fluorescence recovery after photobleaching assay
  - Extraction and biochemical treatments of native PSD
  - AFM measurements
  - Single-molecule tracking
  - Immunostaining
  - AAV production
  - Organotypic slice culture and biolistic transfection
  - AAV injections and acute slice preparation
  - Electrophysiological recording
  - Generation of Shank3_M1718E mutant mice
  - Open field test
  - Three-chamber social interaction test
  - Homecage behaviors
  - Elevated plus maze test
  - Light-dark box test
- QUANTIFICATION AND STATISTICAL ANALYSIS

SUPPLEMENTAL INFORMATION

Supplemental information can be found online at https://doi.org/10.1016/j.cell.2025.07.047.

Received: January 19, 2025
Revised: June 23, 2025
Accepted: July 31, 2025

REFERENCES

1. Boke, E., Ruer, M., Wühr, M., Coughlin, M., Lemaitre, R., Gygi, S.P., Alberti, S., Drechsel, D., Hyman, A.A., and Mitchison, T.J. (2016). Amyloid-like Self-Assembly of a Cellular Compartment. Cell *166*, 637–650. https://doi.org/10.1016/j.cell.2016.06.051.
2. Roovers, E.F., Kaaij, L.J.T., Redl, S., Bronkhorst, A.W., Wiebrands, K., de Jesus Domingues, A.M., Huang, H.Y., Han, C.T., Riemer, S., Dosch, R., et al. (2018). Tdrd6a Regulates the Aggregation of Buc into Functional Subcellular Compartments that Drive Germ Cell Specification. Dev. Cell *46*, 285–301.e9. https://doi.org/10.1016/j.devcel.2018.07.009.
3. Jentoft, I.M.A., Bäuerlein, F.J.B., Welp, L.M., Cooper, B.H., Petrovic, A., So, C., Penir, S.M., Politi, A.Z., Horokhovskyi, Y., Takala, I., et al. (2023). Mammalian oocytes store proteins for the early embryo on cytoplasmic lattices. Cell *186*, 5308–5327.e25. https://doi.org/10.1016/j.cell.2023.10.003.
4. Zaffagnini, G., Cheng, S., Salzer, M.C., Pernaute, B., Duran, J.M., Irimia, M., Schuh, M., and Böke, E. (2024). Mouse oocytes sequester aggregated proteins in degradative super-organelles. Cell *187*, 1109–1126.e21. https://doi.org/10.1016/j.cell.2024.01.031.
5. Kennedy, M.B. (2000). Signal-processing machines at the postsynaptic density. Science *290*, 750–754. https://doi.org/10.1126/science.290.5492.750.
6. Yang, G., Pan, F., and Gan, W.B. (2009). Stably maintained dendritic spines are associated with lifelong memories. Nature *462*, 920–924. https://doi.org/10.1038/nature08577.
7. Dosemeci, A., Weinberg, R.J., Reese, T.S., and Tao-Cheng, J.H. (2016). The Postsynaptic Density: There Is More than Meets the Eye. Front. Synaptic Neurosci. *8*, 23. https://doi.org/10.3389/fnsyn.2016.00023.
8. Hou, F., Sun, L., Zheng, H., Skaug, B., Jiang, Q.X., and Chen, Z.J. (2011). MAVS forms functional prion-like aggregates to activate and propagate antiviral innate immune response. Cell *146*, 448–461. https://doi.org/10.1016/j.cell.2011.06.041.
9. Cai, X., Chen, J., Xu, H., Liu, S., Jiang, Q.X., Halfmann, R., and Chen, Z.J. (2014). Prion-like polymerization underlies signal transduction in antiviral immune defense and inflammasome activation. Cell *156*, 1207–1222. https://doi.org/10.1016/j.cell.2014.01.063.
10. Guo, P., Li, B., Dong, W., Zhou, H., Wang, L., Su, T., Carl, C., Zheng, Y., Hong, Y., Deng, H., et al. (2024). PI4P-mediated solid-like Merlin condensates orchestrate Hippo pathway regulation. Science *385*, eadf4478. https://doi.org/10.1126/science.adf4478.
11. Neumann, M., Sampathu, D.M., Kwong, L.K., Truax, A.C., Micsenyi, M.C., Chou, T.T., Bruce, J., Schuck, T., Grossman, M., Clark, C.M., et al. (2006). Ubiquitinated TDP-43 in frontotemporal lobar degeneration and amyotrophic lateral sclerosis. Science *314*, 130–133. https://doi.org/10.1126/science.1134108.
12. Molliex, A., Temirov, J., Lee, J., Coughlin, M., Kanagaraj, A.P., Kim, H.J., Mittag, T., and Taylor, J.P. (2015). Phase separation by low complexity domains promotes stress granule assembly and drives pathological fibrillization. Cell *163*, 123–133. https://doi.org/10.1016/j.cell.2015.09.015.
13. Yu, H., Lu, S., Gasior, K., Singh, D., Vazquez-Sanchez, S., Tapia, O., Toprani, D., Beccari, M.S., Yates, J.R., 3rd, Da Cruz, S., et al. (2021). HSP70 chaperones RNA-free TDP-43 into anisotropic intranuclear liquid spherical shells. Science *371*, eabb4309. https://doi.org/10.1126/science.abb4309.
14. Li, Q., Babinchak, W.M., and Surewicz, W.K. (2021). Cryo-EM structure of amyloid fibrils formed by the entire low complexity domain of TDP-43. Nat. Commun. *12*, 1620. https://doi.org/10.1038/s41467-021-21912-y.
15. Ittner, L.M., and Götz, J. (2011). Amyloid-beta and tau–a toxic pas de deux in Alzheimer's disease. Nat. Rev. Neurosci. *12*, 65–72. https://doi.org/10.1038/nrn2967.
16. Fitzpatrick, A.W.P., Falcon, B., He, S., Murzin, A.G., Murshudov, G., Garringer, H.J., Crowther, R.A., Ghetti, B., Goedert, M., and Scheres, S.H.W. (2017). Cryo-EM structures of tau filaments from Alzheimer's disease. Nature *547*, 185–190. https://doi.org/10.1038/nature23002.

17. Wegmann, S., Eftekharzadeh, B., Tepper, K., Zoltowska, K.M., Bennett, R. E., Dujardin, S., Laskowski, P.R., MacKenzie, D., Kamath, T., Commins, C., et al. (2018). Tau protein liquid-liquid phase separation can initiate tau aggregation. EMBO J. *37*, e98049. https://doi.org/10.15252/embj.201798049.

18. Hernández-Vega, A., Braun, M., Scharrel, L., Jahnel, M., Wegmann, S., Hyman, B.T., Alberti, S., Diez, S., and Hyman, A.A. (2017). Local Nucleation of Microtubule Bundles through Tubulin Concentration into a Condensed Tau Phase. Cell Rep. *20*, 2304–2312. https://doi.org/10.1016/j.celrep.2017.08.042.

19. Spillantini, M.G., Schmidt, M.L., Lee, V.M., Trojanowski, J.Q., Jakes, R., and Goedert, M. (1997). Alpha-synuclein in Lewy bodies. Nature *388*, 839–840. https://doi.org/10.1038/42166.

20. Tuttle, M.D., Comellas, G., Nieuwkoop, A.J., Covell, D.J., Berthold, D.A., Kloepper, K.D., Courtney, J.M., Kim, J.K., Barclay, A.M., Kendall, A., et al. (2016). Solid-state NMR structure of a pathogenic fibril of full-length human alpha-synuclein. Nat. Struct. Mol. Biol. *23*, 409–415. https://doi.org/10.1038/nsmb.3194.

21. Ray, S., Singh, N., Kumar, R., Patel, K., Pandey, S., Datta, D., Mahato, J., Panigrahi, R., Navalkar, A., Mehra, S., et al. (2020). alpha-Synuclein aggregation nucleates through liquid-liquid phase separation. Nat. Chem. *12*, 705–716. https://doi.org/10.1038/s41557-020-0465-9.

22. Kwiatkowski, T.J., Jr., Bosco, D.A., Leclerc, A.L., Tamrazian, E., Vanderburg, C.R., Russ, C., Davis, A., Gilchrist, J., Kasarskis, E.J., Munsat, T., et al. (2009). Mutations in the FUS/TLS gene on chromosome 16 cause familial amyotrophic lateral sclerosis. Science *323*, 1205–1208. https://doi.org/10.1126/science.1166066.

23. Vance, C., Rogelj, B., Hortobágyi, T., De Vos, K.J., Nishimura, A.L., Sreedharan, J., Hu, X., Smith, B., Ruddy, D., Wright, P., et al. (2009). Mutations in FUS, an RNA processing protein, cause familial amyotrophic lateral sclerosis type 6. Science *323*, 1208–1211. https://doi.org/10.1126/science.1165942.

24. Patel, A., Lee, H.O., Jawerth, L., Maharana, S., Jahnel, M., Hein, M.Y., Stoynov, S., Mahamid, J., Saha, S., Franzmann, T.M., et al. (2015). A Liquid-to-Solid Phase Transition of the ALS Protein FUS Accelerated by Disease Mutation. Cell *162*, 1066–1077. https://doi.org/10.1016/j.cell.2015.07.047.

25. Sawaya, M.R., Hughes, M.P., Rodriguez, J.A., Riek, R., and Eisenberg, D.S. (2021). The expanding amyloid family: Structure, stability, function, and pathogenesis. Cell *184*, 4857–4873. https://doi.org/10.1016/j.cell.2021.08.013.

26. Murray, D.T., Kato, M., Lin, Y., Thurber, K.R., Hung, I., McKnight, S.L., and Tycko, R. (2017). Structure of FUS Protein Fibrils and Its Relevance to Self-Assembly and Phase Separation of Low-Complexity Domains. Cell *171*, 615–627.e16. https://doi.org/10.1016/j.cell.2017.08.048.

27. Lu, J., Cao, Q., Hughes, M.P., Sawaya, M.R., Boyer, D.R., Cascio, D., and Eisenberg, D.S. (2020). CryoEM structure of the low-complexity domain of hnRNPA2 and its conversion to pathogenic amyloid. Nat. Commun. *11*, 4090. https://doi.org/10.1038/s41467-020-17905-y.

28. Xiang, S., Kato, M., Wu, L.C., Lin, Y., Ding, M., Zhang, Y., Yu, Y., and McKnight, S.L. (2015). The LC Domain of hnRNPA2 Adopts Similar Conformations in Hydrogel Polymers, Liquid-like Droplets, and Nuclei. Cell *163*, 829–839. https://doi.org/10.1016/j.cell.2015.10.040.

29. Li, P., Banjade, S., Cheng, H.C., Kim, S., Chen, B., Guo, L., Llaguno, M., Hollingsworth, J.V., King, D.S., Banani, S.F., et al. (2012). Phase transitions in the assembly of multivalent signalling proteins. Nature *483*, 336–340. https://doi.org/10.1038/nature10879.

30. Mittag, T., and Pappu, R.V. (2022). A conceptual framework for understanding phase separation and addressing open questions and challenges. Mol. Cell *82*, 2201–2214. https://doi.org/10.1016/j.molcel.2022.05.018.

31. Zhu, L., Richardson, T.M., Wacheul, L., Wei, M.T., Feric, M., Whitney, G., Lafontaine, D.L.J., and Brangwynne, C.P. (2019). Controlling the material properties and rRNA processing function of the nucleolus using light. Proc. Natl. Acad. Sci. USA *116*, 17330–17335. https://doi.org/10.1073/pnas.1903870116.

32. Heidenreich, M., Georgeson, J.M., Locatelli, E., Rovigatti, L., Nandi, S.K., Steinberg, A., Nadav, Y., Shimoni, E., Safran, S.A., Doye, J.P.K., et al. (2020). Designer protein assemblies with tunable phase diagrams in living cells. Nat. Chem. Biol. *16*, 939–945. https://doi.org/10.1038/s41589-020-0576-z.

33. Ramšak, M., Ramirez, D.A., Hough, L.E., Shirts, M.R., Vidmar, S., Elerščič Filipič, K., Anderluh, G., and Jerala, R. (2023). Programmable de novo designed coiled coil-mediated phase separation in mammalian cells. Nat. Commun. *14*, 7973. https://doi.org/10.1038/s41467-023-43742-w.

34. Harris, K.M., and Weinberg, R.J. (2012). Ultrastructure of synapses in the mammalian brain. Cold Spring Harb. Perspect. Biol. *4*, a005587. https://doi.org/10.1101/cshperspect.a005587.

35. Borczyk, M., Śliwińska, M.A., Caly, A., Bernas, T., and Radwanska, K. (2019). Neuronal plasticity affects correlation between the size of dendritic spine and its postsynaptic density. Sci. Rep. *9*, 1693. https://doi.org/10.1038/s41598-018-38412-7.

36. Holler, S., Köstinger, G., Martin, K.A.C., Schuhknecht, G.F.P., and Stratford, K.J. (2021). Structure and function of a neocortical synapse. Nature *591*, 111–116. https://doi.org/10.1038/s41586-020-03134-2.

37. Matsuzaki, M., Honkura, N., Ellis-Davies, G.C.R., and Kasai, H. (2004). Structural basis of long-term potentiation in single dendritic spines. Nature *429*, 761–766. https://doi.org/10.1038/nature02617.

38. Shen, K., and Meyer, T. (1999). Dynamic control of CaMKII translocation and localization in hippocampal neurons by NMDA receptor stimulation. Science *284*, 162–166. https://doi.org/10.1126/science.284.5411.162.

39. Bosch, M., Castro, J., Saneyoshi, T., Matsuno, H., Sur, M., and Hayashi, Y. (2014). Structural and molecular remodeling of dendritic spine substructures during long-term potentiation. Neuron *82*, 444–459. https://doi.org/10.1016/j.neuron.2014.03.021.

40. Araki, Y., Zeng, M., Zhang, M., and Huganir, R.L. (2015). Rapid dispersion of SynGAP from synaptic spines triggers AMPA receptor insertion and spine enlargement during LTP. Neuron *85*, 173–189. https://doi.org/10.1016/j.neuron.2014.12.023.

41. Malenka, R.C., Kauer, J.A., Perkel, D.J., and Nicoll, R.A. (1989). The impact of postsynaptic calcium on synaptic transmission–its role in long-term potentiation. Trends Neurosci. *12*, 444–450. https://doi.org/10.1016/0166-2236(89)90094-5.

42. Huganir, R.L., and Nicoll, R.A. (2013). AMPARs and synaptic plasticity: the last 25 years. Neuron *80*, 704–717. https://doi.org/10.1016/j.neuron.2013.10.025.

43. Nicoll, R.A. (2017). A Brief History of Long-Term Potentiation. Neuron *93*, 281–290. https://doi.org/10.1016/j.neuron.2016.12.015.

44. Cotman, C.W., Banker, G., Churchill, L., and Taylor, D. (1974). Isolation of postsynaptic densities from rat brain. J. Cell Biol. *63*, 441–455. https://doi.org/10.1083/jcb.63.2.441.

45. Carlin, R.K., Grab, D.J., Cohen, R.S., and Siekevitz, P. (1980). Isolation and characterization of postsynaptic densities from various brain regions: enrichment of different types of postsynaptic densities. J. Cell Biol. *86*, 831–845. https://doi.org/10.1083/jcb.86.3.831.

46. Zeng, M., Chen, X., Guan, D., Xu, J., Wu, H., Tong, P., and Zhang, M. (2018). Reconstituted Postsynaptic Density as a Molecular Platform for Understanding Synapse Formation and Plasticity. Cell *174*, 1172–1187.e16. https://doi.org/10.1016/j.cell.2018.06.047.

47. Zeng, M., Díaz-Alonso, J., Ye, F., Chen, X., Xu, J., Ji, Z., Nicoll, R.A., and Zhang, M. (2019). Phase Separation-Mediated TARP/MAGUK Complex Condensation and AMPA Receptor Synaptic Transmission. Neuron *104*, 529–543.e6. https://doi.org/10.1016/j.neuron.2019.08.001.

48. Shen, Z., Jia, B., Xu, Y., Wessén, J., Pal, T., Chan, H.S., Du, S., and Zhang, M. (2023). Biological condensates form percolated networks with molecular motion properties distinctly different from dilute solutions. eLife *12*, e81907. https://doi.org/10.7554/eLife.81907.

49. Zhu, S., Shen, Z., Wu, X., Han, W., Jia, B., Lu, W., and Zhang, M. (2024). Demixing is a default process for biological condensates formed via phase separation. Science *384*, 920–928. https://doi.org/10.1126/science.adj7066.

50. Liao, Z., Jia, B., Guan, D., Chen, X., Zhang, M., and Tong, P. (2025). Emergent mechanics of a networked multivalent protein condensate. Nat. Commun. *16*, 5237. https://doi.org/10.1038/s41467-025-60345-9.

51. Durand, C.M., Betancur, C., Boeckers, T.M., Bockmann, J., Chaste, P., Fauchereau, F., Nygren, G., Rastam, M., Gillberg, I.C., Anckarsäter, H., et al. (2007). Mutations in the gene encoding the synaptic scaffolding protein SHANK3 are associated with autism spectrum disorders. Nat. Genet. *39*, 25–27. https://doi.org/10.1038/ng1933.

52. Monteiro, P., and Feng, G. (2017). SHANK proteins: roles at the synapse and in autism spectrum disorder. Nat. Rev. Neurosci. *18*, 147–157. https://doi.org/10.1038/nrn.2016.183.

53. De Rubeis, S., Siper, P.M., Durkin, A., Weissman, J., Muratet, F., Halpern, D., Trelles, M.D.P., Frank, Y., Lozano, R., Wang, A.T., et al. (2018). Delineation of the genetic and clinical spectrum of Phelan-McDermid syndrome caused by SHANK3 point mutations. Mol. Autism *9*, 31. https://doi.org/10.1186/s13229-018-0205-9.

54. Leblond, C.S., Nava, C., Polge, A., Gauthier, J., Huguet, G., Lumbroso, S., Giuliano, F., Stordeur, C., Depienne, C., Mouzat, K., et al. (2014). Meta-analysis of SHANK Mutations in Autism Spectrum Disorders: a gradient of severity in cognitive impairments. PLoS Genet. *10*, e1004580. https://doi.org/10.1371/journal.pgen.1004580.

55. Chen, X., Jia, B., Zhu, S., and Zhang, M. (2023). Phase separation-mediated actin bundling by the postsynaptic density condensates. eLife *12*, e84446. https://doi.org/10.7554/eLife.84446.

56. Baron, M.K., Boeckers, T.M., Vaida, B., Faham, S., Gingery, M., Sawaya, M.R., Salyer, D., Gundelfinger, E.D., and Bowie, J.U. (2006). An architectural framework that may lie at the core of the postsynaptic density. Science *311*, 531–535. https://doi.org/10.1126/science.1118995.

57. Wu, H., Chen, X., Shen, Z., Li, H., Liang, S., Lu, Y., and Zhang, M. (2024). Phosphorylation-dependent membraneless organelle fusion and fission illustrated by postsynaptic density assemblies. Mol. Cell *84*, 309–326. e7. https://doi.org/10.1016/j.molcel.2023.11.011.

58. Chen, D.T.N., Wen, Q., Janmey, P.A., Crocker, J.C., and Yodh, A.G. (2010). Rheology of soft materials. Annu. Rev. Condens. Matter Phys. *1*, 301–322. https://doi.org/10.1146/annurev-conmatphys-070909-104120.

59. Fabry, B., Maksym, G.N., Butler, J.P., Glogauer, M., Navajas, D., and Fredberg, J.J. (2001). Scaling the microrheology of living cells. Phys. Rev. Lett. *87*, 148102. https://doi.org/10.1103/PhysRevLett.87.148102.

60. Semmrich, C., Storz, T., Glaser, J., Merkel, R., Bausch, A.R., and Kroy, K. (2007). Glass transition and rheological redundancy in F-actin solutions. Proc. Natl. Acad. Sci. USA *104*, 20199–20203. https://doi.org/10.1073/pnas.0705513104.

61. Sollich, P., Lequeux, F., Hébraud, P., and Cates, M.E. (1997). Rheology of soft glassy materials. Phys. Rev. Lett. *78*, 2020–2023. https://doi.org/10.1103/PhysRevLett.78.2020.

62. Alberti, S., Gladfelter, A., and Mittag, T. (2019). Considerations and Challenges in Studying Liquid-Liquid Phase Separation and Biomolecular Condensates. Cell *176*, 419–434. https://doi.org/10.1016/j.cell.2018.12.035.

63. Diering, G.H., Nirujogi, R.S., Roth, R.H., Worley, P.F., Pandey, A., and Huganir, R.L. (2017). Homer1a drives homeostatic scaling-down of excitatory synapses during sleep. Science *355*, 511–515. https://doi.org/10.1126/science.aai8355.

64. de Vivo, L., Bellesi, M., Marshall, W., Bushong, E.A., Ellisman, M.H., Tononi, G., and Cirelli, C. (2017). Ultrastructural evidence for synaptic scaling across the wake/sleep cycle. Science *355*, 507–510. https://doi.org/10.1126/science.aah5982.

65. Sala, C., Futai, K., Yamamoto, K., Worley, P.F., Hayashi, Y., and Sheng, M. (2003). Inhibition of dendritic spine morphogenesis and synaptic transmission by activity-inducible protein Homer1a. J. Neurosci. *23*, 6327–6337. https://doi.org/10.1523/JNEUROSCI.23-15-06327.2003.

66. Hayashi, M.K., Ames, H.M., and Hayashi, Y. (2006). Tetrameric hub structure of postsynaptic scaffolding protein homer. J. Neurosci. *26*, 8492–8501. https://doi.org/10.1523/JNEUROSCI.2731-06.2006.

67. MacGillavry, H.D., Kerr, J.M., Kassner, J., Frost, N.A., and Blanpied, T.A. (2016). Shank-cortactin interactions control actin dynamics to maintain flexibility of neuronal spines and synapses. Eur. J. Neurosci. *43*, 179–193. https://doi.org/10.1111/ejn.13129.

68. Scheefhals, N., Catsburg, L.A.E., Westerveld, M.L., Blanpied, T.A., Hoogenraad, C.C., and MacGillavry, H.D. (2019). Shank Proteins Couple the Endocytic Zone to the Postsynaptic Density to Control Trafficking and Signaling of Metabotropic Glutamate Receptor 5. Cell Rep. *29*, 258–269. e8. https://doi.org/10.1016/j.celrep.2019.08.102.

69. Choquet, D., and Opazo, P. (2022). The role of AMPAR lateral diffusion in memory. Semin. Cell Dev. Biol. *125*, 76–83. https://doi.org/10.1016/j.semcdb.2022.01.009.

70. Maynard, S.A., Ranft, J., and Triller, A. (2023). Quantifying postsynaptic receptor dynamics: insights into synaptic function. Nat. Rev. Neurosci. *24*, 4–22. https://doi.org/10.1038/s41583-022-00647-9.

71. Chen, L., Chetkovich, D.M., Petralia, R.S., Sweeney, N.T., Kawasaki, Y., Wenthold, R.J., Bredt, D.S., and Nicoll, R.A. (2000). Stargazin regulates synaptic targeting of AMPA receptors by two distinct mechanisms. Nature *408*, 936–943. https://doi.org/10.1038/35050030.

72. Tardin, C., Cognet, L., Bats, C., Lounis, B., and Choquet, D. (2003). Direct imaging of lateral movements of AMPA receptors inside synapses. EMBO J. *22*, 4656–4665. https://doi.org/10.1093/emboj/cdg463.

73. Nair, D., Hosy, E., Petersen, J.D., Constals, A., Giannone, G., Choquet, D., and Sibarita, J.B. (2013). Super-resolution imaging reveals that AMPA receptors inside synapses are dynamically organized in nanodomains regulated by PSD95. J. Neurosci. *33*, 13204–13224. https://doi.org/10.1523/JNEUROSCI.2381-12.2013.

74. Kim, C.A., Gingery, M., Pilpa, R.M., and Bowie, J.U. (2002). The SAM domain of polyhomeotic forms a helical polymer. Nat. Struct. Biol. *9*, 453–457. https://doi.org/10.1038/nsb802.

75. Leblond, C.S., Heinrich, J., Delorme, R., Proepper, C., Betancur, C., Huguet, G., Konyukh, M., Chaste, P., Ey, E., Rastam, M., et al. (2012). Genetic and functional analyses of SHANK2 mutations suggest a multiple hit model of autism spectrum disorders. PLoS Genet. *8*, e1002521. https://doi.org/10.1371/journal.pgen.1002521.

76. Hassani Nia, F., Woike, D., Bento, I., Niebling, S., Tibbe, D., Schulz, K., Hirnet, D., Skiba, M., Hönck, H.H., Veith, K., et al. (2024). Structural deficits in key domains of Shank2 lead to alterations in postsynaptic nanoclusters and to a neurodevelopmental disorder in humans. Mol. Psychiatry *29*, 1683–1697. https://doi.org/10.1038/s41380-022-01882-3.

77. Peça, J., Feliciano, C., Ting, J.T., Wang, W., Wells, M.F., Venkatraman, T.N., Lascola, C.D., Fu, Z., and Feng, G. (2011). Shank3 mutant mice display autistic-like behaviours and striatal dysfunction. Nature *472*, 437–442. https://doi.org/10.1038/nature09965.

78. Schmeisser, M.J., Ey, E., Wegener, S., Bockmann, J., Stempel, A.V., Kuebler, A., Janssen, A.L., Udvardi, P.T., Shiban, E., Spilker, C., et al. (2012). Autistic-like behaviours and hyperactivity in mice lacking ProSAP1/Shank2. Nature *486*, 256–260. https://doi.org/10.1038/nature11015.

79. Nicoll, R.A., and Schulman, H. (2023). Synaptic memory and CaMKII. Physiol. Rev. *103*, 2877–2925. https://doi.org/10.1152/physrev.00034.2022.

80. Walkup, W.G., Mastro, T.L., Schenker, L.T., Vielmetter, J., Hu, R., Iancu, A., Reghunathan, M., Bannon, B.D., and Kennedy, M.B. (2016). A model for regulation by SynGAP-alpha1 of binding of synaptic proteins to PDZ-domain 'Slots' in the postsynaptic density. eLife *5*, e16813. https://doi.org/10.7554/eLife.16813.

81. Chen, X., Jia, B., Araki, Y., Liu, B., Ye, F., Huganir, R., and Zhang, M. (2022). Arc weakens synapses by dispersing AMPA receptors from postsynaptic density via modulating PSD phase separation. Cell Res. *32*, 914–930. https://doi.org/10.1038/s41422-022-00697-9.

82. Suzuki, T. (2011). Isolation of Synapse Subdomains by Subcellular Fractionation Using Sucrose Density Gradient Centrifugation. In Neuroproteomics, K.W. Li, ed. (Humana Press), pp. 47–61. https://doi.org/10.1007/978-1-61779-111-6_4.

83. McCoy, A.J., Grosse-Kunstleve, R.W., Adams, P.D., Winn, M.D., Storoni, L.C., and Read, R.J. (2007). Phaser crystallographic software. J. Appl. Crystallogr. *40*, 658–674. https://doi.org/10.1107/S0021889807021206.

84. Emsley, P., Lohkamp, B., Scott, W.G., and Cowtan, K. (2010). Features and development of Coot. Acta Crystallogr. D Biol. Crystallogr. *66*, 486–501. https://doi.org/10.1107/S0907444910007493.

85. Murshudov, G.N., Skubák, P., Lebedev, A.A., Pannu, N.S., Steiner, R.A., Nicholls, R.A., Winn, M.D., Long, F., and Vagin, A.A. (2011). REFMAC5 for the refinement of macromolecular crystal structures. Acta Crystallogr. D Biol. Crystallogr. *67*, 355–367. https://doi.org/10.1107/S0907444911001314.

86. Afonine, P.V., Grosse-Kunstleve, R.W., Echols, N., Headd, J.J., Moriarty, N.W., Mustyakimov, M., Terwilliger, T.C., Urzhumtsev, A., Zwart, P.H., and Adams, P.D. (2012). Towards automated crystallographic structure refinement with phenix.refine. Acta Crystallogr. D Biol. Crystallogr. *68*, 352–367. https://doi.org/10.1107/S0907444912001308.

87. Williams, C.J., Headd, J.J., Moriarty, N.W., Prisant, M.G., Videau, L.L., Deis, L.N., Verma, V., Keedy, D.A., Hintze, B.J., Chen, V.B., et al. (2018). MolProbity: more and better reference data for improved all-atom structure validation. Protein Sci. *27*, 293–315. https://doi.org/10.1002/pro.3330.

88. Kabsch, W. (2010). Xds. Acta Crystallogr. D Biol. Crystallogr. *66*, 125–132. https://doi.org/10.1107/S0907444909047337.

89. Adams, P.D., Afonine, P.V., Bunkóczi, G., Chen, V.B., Davis, I.W., Echols, N., Headd, J.J., Hung, L.W., Kapral, G.J., Grosse-Kunstleve, R.W., et al. (2010). PHENIX: a comprehensive Python-based system for macromolecular structure solution. Acta Crystallogr. D Biol. Crystallogr. *66*, 213–221. https://doi.org/10.1107/S0907444909052925.

90. Alberti, S., Saha, S., Woodruff, J.B., Franzmann, T.M., Wang, J., and Hyman, A.A. (2018). A User's Guide for Phase Separation Assays with Purified Proteins. J. Mol. Biol. *430*, 4806–4820. https://doi.org/10.1016/j.jmb.2018.06.038.

91. Kinoshita, E., Kinoshita-Kikuta, E., and Koike, T. (2009). Separation and detection of large phosphoproteins using Phos-tag SDS-PAGE. Nat. Protoc. *4*, 1513–1521. https://doi.org/10.1038/nprot.2009.154.

92. Guan, D., Shen, Y., Zhang, R., Huang, P., Lai, P.-Y., and Tong, P. (2021). Unified description of compressive modulus revealing multiscale mechanics of living cells. Phys. Rev. Research *3*, 043166. https://doi.org/10.1103/PhysRevResearch.3.043166.

93. Hertz, H. (1882). Ueber die Berührung fester elastischer Körper. J. Reine Angew. Math. *1882*, 156–171. https://doi.org/10.1515/crll.1882.92.156.

94. Benke, A., Olivier, N., Gunzenhäuser, J., and Manley, S. (2012). Multicolor Single Molecule Tracking of Stochastically Active Synthetic Dyes. Nano Lett. *12*, 2619–2624. https://doi.org/10.1021/nl301018r.

95. Challis, R.C., Ravindra Kumar, S., Chan, K.Y., Challis, C., Beadle, K., Jang, M.J., Kim, H.M., Rajendran, P.S., Tompkins, J.D., Shivkumar, K., et al. (2019). Systemic AAV vectors for widespread and targeted gene delivery in rodents. Nat. Protoc. *14*, 379–414. https://doi.org/10.1038/s41596-018-0097-3.

96. Stoppini, L., Buchs, P.A., and Muller, D. (1991). A simple method for organotypic cultures of nervous tissue. J. Neurosci. Methods *37*, 173–182. https://doi.org/10.1016/0165-0270(91)90128-m.

97. Ran, F.A., Hsu, P.D., Wright, J., Agarwala, V., Scott, D.A., and Zhang, F. (2013). Genome engineering using the CRISPR-Cas9 system. Nat. Protoc. *8*, 2281–2308. https://doi.org/10.1038/nprot.2013.143.

98. Bai, G., Li, H., Qin, P., Guo, Y., Yang, W., Lian, Y., Ye, F., Chen, J., Wu, M., Huang, R., et al. (2023). Ca2+-induced release of IQSEC2/BRAG1 autoinhibition under physiological and pathological conditions. J. Cell Biol. *222*, e202307117. https://doi.org/10.1083/jcb.202307117.

Please cite this article in press as: Jia et al., Shank3 oligomerization governs material properties of the postsynaptic density condensate and synaptic plasticity, Cell (2025), https://doi.org/10.1016/j.cell.2025.07.047

STAR★METHODS

KEY RESOURCES TABLE

REAGENT or RESOURCE	SOURCE	IDENTIFIER
Antibodies		
Mouse monoclonal anti-GluA1	Millipore	Cat#MAB2263; RRID: AB_11212678
Donkey polyclonal anti-mouse IgG (H+L), CF®568	Biotium	Cat#20802; RRID: AB_3678765
Mouse monoclonal anti-CaMKIIα	Abcam	Cat#ab22609; RRID: AB_447192
Rabbit polyclonal anti-CaMKIIα pT286	Abcam	Cat#ab5683; RRID: AB_305050
Rabbit polyclonal anti-SAPAP1	Invitrogen	Cat#PA5-78658; RRID: AB_2736558
HRP-conjugated goat polyclonal anti-mouse IgG (H+L)	Immunoway	Cat#RS0001; RRID: AB_2943495
HRP-conjugated alpaca monoclonal anti-rabbit IgG Fc	Huabio	Cat#HA1031; RRID: AB_3697697
Bacterial and virus strains		
Escherichia coli BL21 (DE3) cells	Invitrogen	Cat#C600003
AAV-hSyn-mirShank-mCherry	This paper	N/A
AAV-hSyn-GFP-miniShank-WT	This paper	N/A
AAV-hSyn-GFP-miniShank-ME	This paper	N/A
Biological samples		
Native PSDs purified from mouse brains	Suzuki[82]	N/A
Chemicals, peptides, and recombinant proteins		
Recombinant protein: PSD-95 (aa 1M-724L, UniProt: P78352)	Zeng et al.[46]	N/A
Recombinant protein: Trx-PSD-95_PSG (aa 309R-724L, UniProt: P78352)	Zeng et al.[46]	N/A
Recombinant protein: Stg_CT (aa 203D-323V, UniProt: Q3ZB20)	Zeng et al.[47]	N/A
Recombinant protein: pi-GKAP (phosphorylated GKAP* AAS)	Wu et al.[57]	N/A
Recombinant protein: GB1-Shank3-WT (6x PSD component)	Zeng et al.[46] and this paper	N/A
Recombinant protein: GB1-Shank3-MA/ME (6x PSD component, M1718A/E)	Zeng et al.[46] and this paper	N/A
Recombinant protein: GB1-Shank3-LW (6x PSD component, L1681W)	Zeng et al.[46] and this paper	N/A
Recombinant protein: GB1-Shank3-dSAM (6x PSD component, lacking 1654G-1730S)	Zeng et al.[46] and this paper	N/A
Recombinant protein: GB1-Shank3-dPh-WT (6x PSD component, 1654G-1730S replaced with 1502V-1577V, Uniprot: P39769)	Zeng et al.[46] and this paper	N/A
Recombinant protein: GB1-Shank3-dPh-LR (6x PSD component, 1654G-1730S replaced with 1502V-1577V, L1561R, Uniprot: P39769)	Zeng et al.[46] and this paper	N/A
Recombinant protein: Homer2 (aa 1M-354N, Uniprot: Q9QWW1)	This paper	N/A
Recombinant protein: Homer1a (aa 1M-186K, UniProt: Q9Z214)	Zeng et al.[46]	N/A
Cy3 succinimidyl ester	AAT Bioquest	Cat#271

(*Continued on next page*)

Please cite this article in press as: Jia et al., Shank3 oligomerization governs material properties of the postsynaptic density condensate and synaptic plasticity, Cell (2025), https://doi.org/10.1016/j.cell.2025.07.047

Continued

REAGENT or RESOURCE	SOURCE	IDENTIFIER
TMR-Halotag Ligand	Promega	Cat#G8251
5-Fluro-2′-deoxyuridine	Sigma-Aldrich	Cat#F0503
Leibovitz L-15 medium	Gibco	Cat#21083027
Glutathione	Sigma-Aldrich	Cat#G4251
Dulbecco's Modified Eagle Medium (DMEM)	ThermoFisher	Cat#12900017
Neurobasal medium	Gibco	Cat#21103-0249
B27	Gibco	Cat#17504044
GlutaMAX™ Supplement	Gibco	Cat#35050061
Penicillin-Streptomycin	Gibco	Cat#15140122
DNaseI	Sigma-Aldrich	Cat#DN25
Trypsin	ThermoFisher	Cat#15090046
Poly D-Lysine (PDL)	Sigma-Aldrich	Cat#P7280
Hyclone™ Defined Fetal Bovine Serum (FBS)	Cytiva	Cat#SH30070.03
Glucose Oxidase from Aspergilus niger	Sigma-Aldrich	Cat#G2133
D-(+)-Glucose	Sigma-Aldrich	Cat#G8270
Catalase from bovine liver	Sigma-Aldrich	Cat#C9322
KCl	Sigma-Aldrich	Cat#P5405
$MgSO_4$	Sigma-Aldrich	Cat#63138
NaH_2PO_4	Sigma-Aldrich	Cat#S9638
$NaHCO_3$	Sigma-Aldrich	Cat#S8875
L-Ascorbic acid	Sigma-Aldrich	Cat#255564
sucrose	Sigma-Aldrich	Cat#S5016
NaCl	Fisher chemical	Cat#S671-3
$CaCl_2{\cdot}2H_2O$	Sigma-Aldrich	Cat#C5080
$CsMeSO_4$	Sigma-Aldrich	Cat#C1426
QX314-chloride	Abcam	Cat#AB120118
HEPES	Sigma-Aldrich	Cat#H7523
Mg-ATP	Sigma-Aldrich	Cat#A9187
Na-GTP	Sigma-Aldrich	Cat#G8877
EGTA	Sigma-Aldrich	Cat#E3889
Spermine tetrahydrochloride	Sigma-Aldrich	Cat#S1141
Picrotoxin	TCI	Cat#C0375
2-Chloroadenosine	Sigma-Aldrich	Cat#C5134
Avertin	Sigma-Aldrich	Cat#T48402
MEM	Gibco	Cat#12360038
HBSS	Gibco	Cat#14170112
Horse Serum	Gibco	Cat#26050088
Critical commercial assays		
Lipofectamine2000 transfection kit	Invitrogen	Cat#11668019
ViaFect	Promega	Cat#E4982
Helios Gene Gun Kit	Bio-Rad	Cat#1652411
Helios Cartridge Kit	Bio-Rad	Cat#1652440
Deposited data		
Shank3-SAM structure	This paper	PDB: 9KSQ
Experimental models: Cell lines		
Human: HeLa cells	ATCC	CCL-2
Human: HEK293T cells	ATCC	CRL-3216

(*Continued on next page*)

Please cite this article in press as: Jia et al., Shank3 oligomerization governs material properties of the postsynaptic density condensate and synaptic plasticity, Cell (2025), https://doi.org/10.1016/j.cell.2025.07.047

Continued

REAGENT or RESOURCE	SOURCE	IDENTIFIER
Experimental models: Organisms/strains		
Rats: SD (Sprague Dawley) Rats	CUHK (The Chinese University of Hong Kong)	N/A
Rats: SD (Sprague Dawley) Rats	Laboratory Animal Center, Fujian Medical University	N/A
Mice: C57BL/6J mice	Laboratory Animal Center, Fujian Medical University	N/A
Mice: Shank3^{M1718E}	Shanghai Model Organisms	Custom order
Oligonucleotides		
Shank3^{M1718E} Forward primer (F1): 5′-TCGGCCATTTCAACAGAAGC -3′	Sangon Biotech	Custom order
Shank3^{M1718E} Reverse primer (R1): 5′-CCCTTACTGTGTGCTGGGTG -3′	Sangon Biotech	Custom order
Recombinant DNA		
Plasmid: 32M3C-PSD-95_FL	Zeng et al.[46]	N/A
Plasmid: 32M3C-PSD-95_PSG	This paper	N/A
Plasmid: 32M3C-Stg_CT	Zeng et al.[47]	N/A
Plasmid: MG3C-GKAP_AAS	Wu et al.[57]	N/A
Plasmid: M3C-GB1-Shank3-WT (GB1-NPDZ-HBS-CBS-SAM)	Zeng et al.[46] and this paper	N/A
Plasmid: M3C-GB1-Shank3-MA	Zeng et al.[46] and this paper	N/A
Plasmid: M3C-GB1-Shank3-ME	Zeng et al.[46] and this paper	N/A
Plasmid: M3C-GB1-Shank3-LW	Zeng et al.[46] and this paper	N/A
Plasmid: M3C-GB1-Shank3-dSAM	Zeng et al.[46] and this paper	N/A
Plasmid: M3C-GB1-Shank3-dPh-WT	Zeng et al.[46] and this paper	N/A
Plasmid: M3C-GB1-Shank3-dPh-LR	Zeng et al.[46] and this paper	N/A
Plasmid: M3C-Homer2	This paper	N/A
Plasmid: M3C-Homer1a	Zeng et al.[46]	N/A
Plasmid: pSM155-mirShank-mCherry	MacGillavry et al.[67]	N/A
Plasmid: pSM155-mirShank-miRFP670	This paper	N/A
Plasmid: pCMV-GFP	This paper	N/A
Plasmid: pCMV-GFP-Shank3^{re}-WT	This paper	N/A
Plasmid: pCMV-GFP-Shank3^{re}-MA	This paper	N/A
Plasmid: pCMV-GFP-Shank3^{re}-ME	This paper	N/A
Plasmid: pCMV-GFP-Shank3^{re}-dPh-WT	This paper	N/A
Plasmid: pCMV-GFP-Shank3^{re}-dPh-LR	This paper	N/A
Plasmid: pCMV-HaloTag-Shank3^{re}-WT	This paper	N/A
Plasmid: pCMV-HaloTag-Shank3^{re}-MA	This paper	N/A
Plasmid: pCMV-HaloTag-Shank3^{re}-ME	This paper	N/A
Plasmid: pAAV-hSyn-mirShank-mCherry	This paper	N/A
Plasmid: pAAV-hSyn-GFP-miniShank-WT	This paper	N/A
Plasmid: pAAV-hSyn-GFP-miniShank-ME	This paper	N/A
Software and algorithms		
Origin7.0	OriginLab	http://www.originlab.com/
PyMOL	PyMOL	http://www.pymol.org/
ImageJ	NIH	https://imagej.net/ij/
GraphPad Prism	GraphPad Software Inc	http://www.graphpad.com/scientific-software/prism/

(*Continued on next page*)

Please cite this article in press as: Jia et al., Shank3 oligomerization governs material properties of the postsynaptic density condensate and synaptic plasticity, Cell (2025), https://doi.org/10.1016/j.cell.2025.07.047

Continued

REAGENT or RESOURCE	SOURCE	IDENTIFIER
ASTRA6	Wyatt	http://www.wyatt.com/products/software/astra.html
Matlab	MathWorks	https://ww2.mathworks.cn/products/matlab.html
Phaser	McCoy et al.[83]	https://smb.slac.stanford.edu/facilities/software/ccp4/html/phaserwiki/index.html
Coot	Emsley et al.[84]	https://www2.mrc-lmb.cam.ac.uk/personal/pemsley/coot/
Refmac5	Murshudov et al.[85]	https://www2.mrc-lmb.cam.ac.uk/groups/murshudov/content/refmac/refmac.html
Phenix.refine	Afonine et al.[86]	https://phenix-online.org/documentation/reference/refinement.html
MolProbity	Williams et al.[87]	http://molprobity.biochem.duke.edu/
EthoVision XT	Noldus	https://noldus.com/ethovision-xt
Igor Pro 6.37	WaveMetrics	https://www.wavemetrics.com/
SMT analysis algorithms	Shen et al.[48]	https://github.com/NeoLShen/Code-for-phase-simulation-and-HMM-analysis

EXPERIMENTAL MODEL AND STUDY PARTICIPANT DETAILS

Animals

For electrophysiology recording assays, all mice (wild type C57BL/6J) and rats (wild type Sprague Dawley) were kept in individual ventilated cages under a 12-hour light-dark cycle with free access to food and water, and the room temperature was maintained at 24°C. All the experimental procedures on animals were approved by the Institutional Animal Care and Use Committee of Fujian Medical University. For electrophysiological recordings, brain slices were prepared P7-P9 rats for basal AMPAR transmission or from P18-P21 mice for LTP measurements. Both male and female animals were included. We used 6–10 animals to obtain individual complete dataset.

For Shank3^{M1718E} mice and their wild type littermate, all experimental procedures were conducted following protocols approved by the Institutional Animal Care and Use Committee (IACUC) of the animal core facility at Huazhong University of Science and Technology, Wuhan, China. Mice were housed in groups of three to five per cage under a 12-hour light-dark cycle (lighting from 8:00 to 20:00) with food and water available ad libitum, at a consistent ambient temperature (21 ± 1°C) and humidity (50 ± 5%). All tests were performed during the light phase. The mice were handled daily by experimenters for at least 3 days and were then transferred to the testing room for a 1-hour acclimation period before starting the experiments. Male mice aged P150 ± 7 were used for behavioral testing.

Primary hippocampal neuron culture

Primary hippocampal neuron cultures were prepared from embryonic day 19 (E19) Sprague Dawley rats hippocampi. Dissociated cells were plated on poly-D-lysine (PDL) coated coverslips (for fixed sample) or glass bottom petri dish (for live cell imaging, TKO-P351173-413, MatTek) in neurobasal media (Gibco) supplemented with 1% penicillin-streptomycin (10,000 U/ml) (Gibco), 1% GlutaMax Supplement (Gibco), 2% B27 Supplement (Gibco) and 10% fetal bovine serum (FBS, Hyclone). Four hours after plating, the medium was replaced with medium lacking FBS. Neurons were maintained in an incubator at 37°C with 5% CO_2, and the medium was changed every three days over the duration of the culture. Especially, at DIV7, 2.5 μM 5-Fluoro-2'-deoxyuridine (FdU, final concentration) was applied into culture media to inhibit proliferation of glia. Generally, cells were transfected at DIV16 with Lipofectamine 2000 (Invitrogen) in accordance with manufacture's manual. After 5-6 days, cells were subject to live cell imaging or fixed with 4% (vol/vol) paraformaldehyde (PFA) together with 4% (wt/vol) sucrose in 1x PBS (pH 7.5), and then mounted on slides for confocal imaging.

METHOD DETAILS

DNA constructs

DNA fragments encoding recombinant proteins were generated via the standard PCR-based methods and inserted into pET-based vectors containing N-terminal His_6- or TRX-His_6-tag each followed by an HRV-3C protease cleavage site. Sequences of recombinant proteins were described in our previous studies[46,47,57]: Stg, 203D-323V, NP_031609 (NCBI); PSD-95, 1M-724L, P78352-1 (Uniprot),

PSG boundary is 309R-724L; GKAP (3GBR-CT), 328Q-421S+916Q-992L, S/T residue to G outside 3rd R2, Q9D415-1 (Uniprot)[57]; Shank3 (NPDZ-HBS-CBS-SAM), 533D-665R+1294D-1323P+1400A-1426P+1654G-1730S, Q4ACU6-1 (Uniprot), GB1 tag on the N-terminus to increase protein solubility; Homer2, 1M-354N, Q9QWW1 (Uniprot); Homer1a, 1M-186K, Q9Z214-3 (Uniprot). dPh_SAM (Uniprot: P39769, 1502V-1577V) DNA fragment was synthesized from BGI. Shank-dPh and Shank3re-dPh DNA fragments were generated via PCR and the Shank3_SAM domain (1654G-1730S) was replaced with dPh_SAM (1502V-1577V). For expressions of corresponding proteins in cultured neurons and hippocampal slices, DNA fragments were inserted downstream of the CMV promoter. Pan-Shank knockdown and rescue constructs were gifts from Dr. Harold MacGillavry and were described previously.[67,68] For the Shank3 localization assay and the FRAP assays in Figures 3 and 5, GFP-tagged Shank3 full length (mouse, Q4ACU6-1, Uniprot) or its variants were co-transfected with pSM155-mirShank-mCherry. For Shank3 single molecule tracking assay in Figure 3F, HaloTag-Shank3 or its variants were co-transfected with pSM155-mirShank-iRFP670. For GluA1 single molecule tracking assay in Figures 4E and 5H, GFP-Shank3 or its variants were co-transfected with pSM155-mirShank-iRFP670. For AMPAR basal transmission assay in Figures 6A–6F, GFP-Shank3 and its variants were co-transfected with pSM155-mirShank-mCherry. For AAV preparations, mirShank-mCherry, GFP, GFP-miniShank-WT and GFP-miniShank-ME were constructed and inserted to pAAV-hSyn-3xFLAG-WPRE (Addgene # 127862) between BamHI and EcoRI sites. All constructs were verified by DNA sequencing.

The full-length *SHANK3* is too large for efficient AAV-based gene delivery to neurons in cultures or *in vivo*. Thus, we created *miniShank3* by removing several segments encoding unstructured regions with no known functions. The miniShank3 contains N-terminal domain and ankyrin repeats which interacts with CaMKII, Ras/Rap, the PDZ domain specifically binding to target proteins such as SAPAPs, the proline-rich region containing the Homer binding sequence (HBS) and cortactin-binding sequence (CBS), and the SAM domain capable of forming homo-oligomer (Figure 6G2). The miniShank3 construct created contains all known protein-interacting domains/motifs. The construction for miniShank3 includes residues 1-376 (NTD-ANK), 533-665 (N-PDZ), 1294-1323 (HBS), 1400-1426 (CBS) and 1654-1730 (linker-SAM) (Q4ACU6-1, Uniprot).

Protein expression and purification

Recombinant proteins were expressed in Escherichia coli BL21-CodonPlus (DE3)-RIL (Agilent) in auto induction LB medium (AIMLB0210, FORMEDIUM) at 16 °C overnight after cells were cultured at 37 °C to OD_{600} between 0.6-0.8. The boundaries and purification protocols of PSD proteins (Stg cytosolic tail, PSD-95 full length and PSG, GKAP with one site phosphorylation, Shank3, and Homer2) were described previously.[46,47,57] An Asn1315Asp mutation in the Homer-binding site (HBS) was introduced in the recombinant Shank3 proteins to enhance Shank-Homer interaction for *in vitro* phase separation studies described in Figures 1, 2, 4 and 5. For Shank-dSAM, aa1654-1730 was truncated from Shank3.

Generally, each recombinant protein was purified using a nickel-NTA agarose affinity column followed by a size-exclusion chromatography (Superdex 200 or Superdex 75) with a column buffer containing 50 mM Tris, pH 8.0, 100 mM NaCl, 1 mM EDTA, 1 mM DTT. After affinity tag was cleaved, the protein was purified by another round of size-exclusion chromatography with a column buffer containing 50 mM Tris, pH 8.0, 100 mM NaCl, 1 mM EDTA, 1 mM DTT. Specifically, a column buffer containing 50 mM Tris, pH 8.0, 300 mM NaCl, 1 mM EDTA, 1mM DTT was used for purification of Homer2 during the whole purification process.

For purification of PSD-95, after size-exclusion chromatography by Superdex 200 following cleavage by HRV3C protease at 4°C overnight, a monoQ ion-exchange chromatography was applied to remove Trx-His_6, small amount of DNA contamination and degraded proteins. Proteins were exchanged into a buffer containing 50 mM Tris, pH 8.0, 100 mM NaCl, 1 mM EDTA, 1 mM DTT. For purification of Stg, cells were grown in LB medium at 37 °C until OD_{600} around 0.8 before induction of protein expression by 0.5 mM IPTG at 37 °C for 3 hours. Proteins eluted from the affinity column were then purified by Superdex 75 size-exclusion chromatography with a column buffer containing 50 mM Tris, pH 8.0, 300 mM NaCl, 1 mM EDTA, 1 mM DTT. After affinity tag cleavage by HRV3C protease, a monoS ion-exchange chromatography was used to remove the Trx-His_6 tag. Proteins were exchanged into a working buffer containing 50 mM Tris, pH 8.0, 100 mM NaCl, 1 mM EDTA, 1 mM DTT by a HiTrap desalting column.

Protein crystallography and structure determination

Crystal of Shank3_SAM WT was obtained by using the mixture of GB1-Shank3_SAM WT (400 μM) with 3C protease (0.2 μM, to cleave the GB1 tag) directly for crystallization in a crystallization buffer (0.2 M Calcium chloride dihydrate, 0.1 M Sodium acetate trihydrate pH 4.6, 20% v/v 2-Propanol) by sitting-drop vapor-diffusion at 289K. Diffraction data were collected at the Shanghai Synchrotron Radiation Facility (BL19U) at 100K. Data were processed and scaled using XDS.[88]

The crystal structure was determined by molecular replacement with the model of Shank3_SAM ME (PDB: 2F3N[56]) using PHASER.[83] Further manual model building and refinement of the structures were completed iteratively using Coot[84] and PHENIX.[89] The final models were validated by MolProbity and the statistics are summarized in Table S1. The structure figures were prepared with PyMOL (http://www.pymol.org). The PDB accession code is 9KSQ for Shank3_SAM WT crystal structure.

Protein fluorescence labeling

Highly purified proteins were exchanged into a HEPES buffer (containing 20 mM HEPES, pH 7.5, 300 mM NaCl, 1 mM EDTA and 1 mM DTT) and concentrated to 5-10 mg/mL. Cy3 NHS Ester (AAT Bioquest) were dissolved by DMSO to make stock solutions at the concentration of 10 mg/mL. Dye and the protein to be labeled were mixed at a molar ratio of 1:1 and the reaction lasted for 2 hours at room temperature. Reaction was quenched by 200 mM Tris, pH 8.2. The fluorophores and other small molecules were

Please cite this article in press as: Jia et al., Shank3 oligomerization governs material properties of the postsynaptic density condensate and synaptic plasticity, Cell (2025), https://doi.org/10.1016/j.cell.2025.07.047

removed from the proteins by passing the reaction mixture through a HiTrap desalting column with buffer containing 50 mM Tris, pH 8.0, 100 mM NaCl, 1 mM EDTA, 1 mM DTT.

Size-exclusion chromatography coupled with multi-angle light scattering assay

The size exclusion chromatography coupled with multi-angle light scattering (SEC-MALS) system is composed of a static light scattering detector (MiniDawn, Wyatt), a differential refractive index detector (Optilab, Wyatt), and an AKTA purifier (GE Healthcare). 100 μL sample was injected into a Superose 6 Increase 10/300 GL column pre-equilibrated with a column buffer containing 50 mM Tris, pH 8.0, 100 mM NaCl, 1 mM EDTA, 1 mM DTT. Data were analyzed by the ASTRA6 (Wyatt) software and fitted molecular weight was obtained.

Phase separation sedimentation and imaging assay

Proteins were prepared in buffer containing 50 mM Tris, pH 8.0, 100 mM NaCl, 1 mM EDTA, and 1 mM DTT. Proteins were then mixed or diluted with buffer to designed combinations and concentrations.

For sedimentation assay, typically, the final volume of each reaction was 50 μL. After 10-min equilibrium at room temperature, protein samples were subjected to sedimentation at 16,873g for 10 mins at 25 °C on a table-top temperature-controlled micro-centrifuge. After centrifugation, the supernatant and pellet were immediately separated into two tubes. The pellet fraction was thoroughly resuspended with the same buffer to the equal volume as the supernatant fraction. Proteins from both fractions were analyzed by SDS-PAGE with Coomassie blue staining. Band intensities were quantified using the ImageJ software. Pellet percentage is defined as I_p / (I_p+I_s) * 100%, where I_p and I_s are intensities of pellet fraction and supernatant fraction, respectively.

For imaging assay, protein samples were injected into a homemade flow chamber (comprised of a glass slide sandwiched by a coverslip with one layer of double-sided tape as a spacer) for DIC (Nikon Ni-U upright fluorescence microscope) and fluorescent imaging (Zeiss LSM880 confocal microscope) at room temperature and incubated for 10 min before imaging. Glasses were washed by Hellmanex III cleaning solution (Hellma Analytics) and thoroughly rinsed with MilliQ H_2O before chamber making. Images were analyzed by the ImageJ software.

Fluorescence recovery after photobleaching assay

Fluorescence recovery after photobleaching (FRAP) assay was performed on a Zeiss LSM 880 confocal microscope. For FRAP on PSD condensates, a circle region with diameter around 2 μm in the center of droplet was selected as region of interest (ROI) for bleaching and recording. The imaging interval is 10 seconds, and recovery was recorded for 10 minutes. Fluorescence intensity difference between prebleaching and at time 0 (the time point right after photobleaching pulse) was normalized to 100%. For FRAP assays on Shank-dPh-containing condensates, protein mixtures were injected into a homemade PEG-coated chambers[90] to avoid severe wetting phenomenon of Shank-dPhLR-containing condensates during the FRAP assay. The FRAP assay is conducted after 20-minute incubation for droplet rounding process. Round droplets with diameter ~10 μm were selected for FRAP assay.

For FRAP on neurons, live cells grown on glass bottom culture dish (MatTek) were maintained at 37 °C with 5% CO_2 for imaging. GFP-Shank3 puncta in dendritic spine were selected as ROI for bleaching and recording. The imaging interval is 5 seconds, and recovery was recorded for 120 seconds. The fluorescent intensity difference between pre-bleaching and at time 0 was normalized to 100%.

Extraction and biochemical treatments of native PSD

PSD was purified from C57BL/6 mouse brain tissue according to previous study.[82] Brains were homogenized by a motor-operated Telflon/glass homogenizer and centrifuged at 1,400 g for 10 mins to remove the nuclear components. The supernatant was further centrifuged at 17,300 g for 10 mins to obtain crude synaptosomes, which was then layered on the discrete sucrose density gradient (1.0 M/1.4 M sucrose) and centrifuged at 25,000 rpm for 70 mins (SW28 rotor). The band in the interface between 1.0 and 1.4 M sucrose layer was collected and lysed by osmotic shock in the presence of 0.5% Triton-X. The detergent-insoluble fraction was collected by 48,200 g centrifugation for 20 mins and further purified by discrete sucrose density gradient centrifugation (1.0 M/1.5 M/2.1 M sucrose, 40,000 rpm for 120 mins with SW40Ti rotor). The PSD enriched in the interface between 1.5 and 2.1 M sucrose layer was diluted with cold ddH_2O. Finally, PSD was collected by centrifugation at 11,000 g for 20 mins and resuspended in 50 mM HEPES buffer, pH 7.4. The concentration of PSD was measured by Bradford Assay.

CaMKII activation and endogenous protein phosphorylation in native PSD were prepared by incubating 0.5 mg/mL native PSD with the buffer containing 50 mM Tris, pH 8.0, 100 mM NaCl supplemented with 3 μM CaM, 10 mM $MgCl_2$, 1 mM ATP, 5 mM DTT, 1 mM $CaCl_2$ at room temperature for 20 mins. Dephosphorylation of endogenous protein in native PSD was performed by incubating 0.5 mg/mL native PSD with the buffer containing 50 mM Tris, pH 8.0, 100 mM NaCl supplemented with 10 μM λ-phosphatase (λ-PPase) and 0.5 mM $MnCl_2$ at room temperature for 1 h. The reaction was stopped by adding SDS-PAGE loading buffer. The phosphorylation state of CaMKIIα was analyzed by SDS-PAGE or Phos-tag gel[91] probed with antibodies, including anti-CaMKIIα (mouse, ab22609, abcam, 1:10,000 dilution) and anti-CaMKIIα-pT286 (rabbit, ab5683, abcam, 1:1,000 dilution). The phosphorylation state of SAPAP1 was analyzed by SDS-PAGE or Phos-tag gel probed with anti-SAPAP1 antibody (rabbit, PA55-78658, Invitrogen, 1:2,000 dilution). HRP-conjugated anti-mouse IgG (H+L) antibody (goat, RS0001, Immunoway, 1:20,000 dilution) and HRP-conjugated anti-rabbit IgG Fc antibody (alpaca, HA1031, Huabio, 1:50,000 dilution) were used for bands visualization.

Please cite this article in press as: Jia et al., Shank3 oligomerization governs material properties of the postsynaptic density condensate and synaptic plasticity, Cell (2025), https://doi.org/10.1016/j.cell.2025.07.047

AFM measurements

The mechanical measurements for 4x PSD were performed on an atomic force microscope (MFP-3D, Asylum Research) supplemented with a colloidal probe. The colloidal probe was prepared by attaching a glass sphere of radius $R_1 \sim 7.5\ \mu m$ onto the front end of a tipless AFM cantilever (CSC37, Micromasch) as described previously.[46,50,92] The spring constant $k = 0.3$ N/m of the cantilever was calibrated in situ during the force measurements using thermal power spectral density method.[46,50,92] The probe was also coated with a layer of poly(L-lysine)-graft-poly(ethylene glycol) (SuSoS AG) to minimize the protein absorption on the probe and reduce the adhesion between the probe and the PSD condensates.

In the force indentation measurements, the probe was brought into contact with the droplet by AFM at each velocity (e.g., $v = 5\ \mu m/s$ and so on) and then retracted from the droplet, during which the droplet responding force $F(\delta)$ as the function of the probe indentation depth δ were captured (see Figures 1J, 1K). The approach force indentation curves for the 4x PSD were found to be well described by the Hertz contact model,[46,93] which gives $F = 16/9 \cdot ER^{1/2}\delta^{3/2}$, where E is the apparent elastic modulus and $R = 1/(1/R_1 + 1/R_2)$ is the reduced radius with R_1 and R_2 being the radius of the probe and the droplet respectively. The elastic modulus E of 4x PSD condensates with different Shank mutations were obtained by fitting the measured force indentation curves with the Hertz model. The measured E characterizes the apparent stiffness (or softness) of the 4x PSD condensates and measures their ability to withstand external deformation. The force indentation measurements were repeated on multiple 4x PSD droplets and at different velocities v.

In the force relaxation measurements, the probe was brought into contact with the droplet at a high velocity $v = 100\ \mu m/s$. When the droplet restoring force reaches the preset value F_0 (at $3 \sim 10$ nN), the probe halted and was held at a fixed position on the droplet. This operation thus imposed an instantaneous and constant indentation δ_0 on the 4x PSD condensates, and the subsequent force evolution $F(t)$ over time was recorded from 10^{-4} s to 10 s. Due to the viscoelasticity of 4x PSD condensates, the measured force gradually decreased over time. The normalized force relaxation $F(t)/F_0$ from multiple 4x PSD droplets were fitted by Eq1. The force relaxation measurements were performed for multiple 4x PSD condensates in at least two different batches of experiments and the curves in Figure 2H is the average of all relaxation curves from all different measured condensates.

Single-molecule tracking

Single-molecule tracking in the reconstituted PSD condensate

Reconstituted PSD condensates with protein of interest (POI) labelled with Cy3 fluorescent dye in the imaging buffer (50 mM Tris, pH 8.0, 100 mM NaCl, 1 mM EDTA and 1 mM DTT supplemented with 0.5% D-glucose (Sigma, G8270), 0.056 mg/mL glucose oxidase (Sigma, G2133-50KU), 4 μg/mL catalase (Sigma C9322-10G), and 14.3 mM β-mercaptoethanol) were transferred into a homemade chamber and loaded onto a Zeiss Elyra7 microscope. A wide field image with a low laser power was captured before tracking. A bleaching process was performed with 100% of 561 nm laser power to eliminate overlapped single molecule signals followed by 50% of 561 nm laser power to stochastically emit Cy3 single molecule fluorescence with long on time. Each single molecule tracking experiment was recorded with 3,000 frames of images with an exposure time of 30 ms per image. Definite-focus system was on during the imaging process. All data were collected within 1 hour imaging session for each sample. Cy3 label ratio: 0.035% for PSD scaffold proteins Shank and PSD-95-PSG, 0.35% for the client protein Stg.

Single-molecule tracking in living neurons

Living neuron samples stained with cell permeable HaloTag TMR ligand (G8251, Promega) for HaloTag-Shank tracking or with GluA1-NTD antibody (MAB2263, Millipore) for GluA1 tracking were transferred to the Leibovitz L-15 medium (Cat #21083027, Gibco) supplemented with 10 mM glutathione (G4251, Sigma-Aldrich)[94] and loaded onto a Zeiss Elyra7 microscope with a live cell supporting system. During the imaging process, the system temperature was maintained at 37.0°C, and the CO_2 level was maintained at 5%. A wide field image with low laser power was captured before tracking, which will be used as the reference to align the tracks with the region of interest. A bleaching process was performed with 50% of 561 nm laser power to eliminate overlapped single molecule signals followed by 20% of 561 nm laser power to stochastically emit CF568 or TMR single molecule fluorescence with long on time. Each single molecule tracking experiment was recorded with 2,000 frames of images with an exposure time of 30 ms for each image. Definite-focus system was on during the imaging process. All data were collected within 1 hour imaging session for each sample.

Single-molecule tracking analysis

Raw data for the living neuron and the reconstituted PSD condensates tracking experiments were first processed with the software installed on the ZEISS Elyra7 microscope. The threshold of the signal to noise ratio was set as 5.0 and the overlapped signals were recognized as multiple localizations. All single molecule localizations were firstly assigned into different trajectories with limited track assignment error by using adaptive search range between constitutive frames. The trajectories were then fitted by a two-state diffusion model with different diffusion coefficient using maximum likelihood estimation. Mobile ratio was defined as the ratio of the number of steps in faster diffusion state and the number of total steps in all trajectories in each sample. The apparent diffusion coefficient (D) was fitted from the mean squared displacement (MSD) within 1 second with equation MSD=4Dt. All the single molecule tracking analysis was performed with a customized program as described previously[48] and included in key resource table.

Immunostaining

For HaloTag-Shank single-molecule tracking in living neuron, cell permeable HaloTag TMR Ligand (G8251, Promega, 1:500 dilution) was applied in culture media supplemented with 1% (vol/vol) FBS at 37°C for 15 minutes, followed by twice of washing with culture

Please cite this article in press as: Jia et al., Shank3 oligomerization governs material properties of the postsynaptic density condensate and synaptic plasticity, Cell (2025), https://doi.org/10.1016/j.cell.2025.07.047

media. Cells were then incubated at 37°C to wash out unbound ligands, followed by another replacement of warm culture medium for single molecule tracking assay. For labeling HaloTag-Shank expressed in Hela cells, cell permeable HaloTag TMR Ligand (G8251, Promega) was diluted in culture media supplemented with 1% (vol/vol) FBS to 1:2,000 and incubated with cells at 37°C for 20 minutes, followed by twice of washing with culture media. Cells were then incubated at 37°C to wash out unbound ligands and fixed by PFA for confocal imaging.

For AMPA receptor single-molecule tracking assay in living neuron, anti-GluA1-NT antibody (MAB2263, Sigma-Aldrich, 1:500 dilution) was applied in culture media supplemented with 1% (vol/vol) FBS at 37 °C for 15 minutes, followed by twice of washing with culture media. CF568-conjugated secondary antibody (#20802, Biotium, 1:500 dilution) was then applied in culture media supplemented with 1% (vol/vol) FBS at 37 °C for 15 minutes. After twice of washing with culture media, the cells were subject for single molecule tracking assay.

AAV production

Recombinant AAVs were generated according to established protocols.[95] In brief, HEK293T cells were triple transfected using polyethylenimine; virus was collected after 120 h from both cell lysates and media and purified over iodixanol (OptiPrep, Sigma-Aldrich).

Organotypic slice culture and biolistic transfection

Organotypic hippocampal cultured slices were obtained from 6- to 8-day-old rat pups.[96] Biolistic transfection was made on DIV1 after sectioning by Helios Gene Gun with 1 μm DNA-coated gold particles (BioRad). When coexpressing two different plasmids, gold particles were coated with equal amounts of each plasmid expressing different fluorescent markers. The observed frequency of coexpression was nearly 100%. Slices were maintained at 34°C and the medium was changed every 2 days. Typically, slices were used for electrophysiological recordings at DIV6-8.

AAV injections and acute slice preparation

According to different experiments, AAV viruses were diluted to different concentrations with PBS and were injected into the ventricle region at P0 (C57BL/6J mice). About 1 μL of viral solution was injected into the ventricle. Injected pups were returned to home cage and acute slices were collected for electrophysiological recording about two weeks later. Mice of P18 to P21 were anesthetized with 2.5% avertin, decapitated, and the brain dissected free. The whole brain was sliced into 300-μm transverse slices in chilled high sucrose cutting solution using the Leica VT1000 Vibratome (Leica); Cutting solution (in mM): 2.5 KCl, 7 $MgSO_4$, 1.25 NaH_2PO_4, 25 $NaHCO_3$, 7 glucose, 210 sucrose, 1.3 ascorbic acid, 3 sodium pyruvate. Slices were transferred into external solutions and recovered at 34°C for 45 minutes to 1 hour and then incubated at room temperature. Solutions were continuously gassed with 95% O_2/5% CO_2.

Electrophysiological recording

Individual slice was transferred to a chamber mounted in an Olympus BX51WI upright microscope and perfused with external solution (2.5 ml/min). External solution (in mM): 119 NaCl, 2.5 KCl, 4 $CaCl_2$, 4 $MgCl_2$, 1 NaH_2PO_4, 26.2 $NaHCO_3$, 11 glucose, bubbled continuously with 95% O_2/5% CO_2. Dual whole-cell voltage clamp recordings were obtained from both transfected neurons and neighboring control neurons in the CA1 region. Pyramidal neurons were identified by location and morphology and transfected neurons identified by epifluorescence. All recordings were made at 20–25°C. Internal solution (in mM): 135 $CsMeSO_4$, 8 NaCl, 10 HEPES, 5 QX314-Cl, 4 Mg-ATP, 0.3 Na-GTP, 0.3 EGTA, 0.1 spermine. Osmolarity was adjusted to 290–295 mOsm and pH was buffered at 7.3–7.4. Synaptic currents were evoked every 10 s with bipolar stimulating electrodes placed in stratum radiatum. To record evoked EPSCs, picrotoxin (100 μM) was added to block inhibitory currents and 2-chloroadenosine (4 μM) was used to control epileptiform activity. For recording of AMPAR EPSCs, the cell membrane was held at −70 mV, while for NMDAR EPSCs, the cell membrane was held at +40 mV. To record LTP, picrotoxin (100 μM) was added to the external solution; after recording a stable 3- to 5-min baseline, LTP is induced by stimulating at 2 Hz for 90 s with holding at 0 mV. Current responses were collected by a Multiclamp 700B amplifier (Axon Instruments), filtered at 2 kHz, and digitized at 10 kHz. Series resistance was monitored on-line, and cells with series resistance larger than 20 MOhm were excluded.

Generation of Shank3_M1718E mutant mice

The $Shank3^{M1718E}$ mutant was generated utilizing the CRISPR/Cas9 genome editing technique as outlined in previous methodologies.[97] Cas9 mRNA, gRNA, and donor DNA were microinjected into fertilized eggs of C57BL/6J mice to produce F0 generation mice. F0 mice with positive PCR product sequencing results were mated with C57BL/6J mice, yielding four positive F1 generation mice. Genotyping was performed using PCR amplification and sequencing. Primers used for genotyping were as follows:

- Forward primer (F1): 5'- TCGGCCATTTCAACAGAAGC -3'
- Reverse primer (R1): 5'-CCCTTACTGTGTGCTGGGTG -3'

Please cite this article in press as: Jia et al., Shank3 oligomerization governs material properties of the postsynaptic density condensate and synaptic plasticity, Cell (2025), https://doi.org/10.1016/j.cell.2025.07.047

Open field test

The test arena was a square enclosure (40 cm × 40 cm × 40 cm) divided into peripheral and central zones. The periphery of the arena was defined as the area within 6 cm adjacent to the walls of the chamber and the central area of the open field was defined as the central one-ninth of the total area. Mice were individually placed in the center of the arena and allowed to explore freely for 5 minutes. Their movements were recorded using an overhead camera and analyzed with behavioral tracking software (e.g., EthoVision XT). Metrics such as total moving distance, average speed, time spent in the peripheral area, and time spent in the central area were extracted for analysis.

Three-chamber social interaction test

The social test apparatus consisted of a transparent acrylic box (40 cm × 20 cm × 21.5 cm) with partitions dividing the box into three chambers. There is a 5 cm opening between each chamber which can be closed or opened with an operated door. The wire cages used to contain the stranger mice were cylindrical, 20 cm in height, a bottom diameter of 10 cm with the bars spaced 1 cm apart to allow for air exchange while preventing direct physical interactions.

In the habituation session, mice were placed in the middle chamber of the apparatus with two empty containers in the side chambers and allowed to explore freely for 5 minutes to assess baseline exploration. Following a delay period of 1 hour, mice underwent a 5-minute test session to evaluate social preference where an age-, sex-, and strain-matched unfamiliar WT mouse was placed in one of the containers to serve as the social stimulus. After another delay period of 1 hour, a second age-, sex-, and strain-matched unfamiliar WT mouse was placed in the other container to serve as a new social stimulus, and mice underwent another 5-minute test session. The positioning of containers was counterbalanced throughout all experiments to avoid bias.

Mouse interactions were tracked and analyzed using behavioral tracking software (e.g., EthoVision XT). During the test sessions, interaction behavior was defined as a mouse approaching its nose within 3 cm of the container. The social preference discrimination index was calculated as (N - F) / (N + F), where N represents the time spent interacting with the novel mouse and F represents the time spent interacting with the familiar mouse. This index provided a measure of the mouse's preference for social novelty, reflecting sociability and social memory. Times were analyzed using automated tracking software to ensure accuracy and consistency. The testing environment, including lighting and temperature, was kept consistent for all mice to minimize variability.

Homecage behaviors

Homecage behaviors assay is performed as previously reported.[98] Individual mice were housed and continuously monitored in PhenoTyper home cages (40 × 40 × 40 cm; Noldus), with ad libitum access to food and water. Animal activity was recorded using an integrated system combining overhead video tracking and infrared beam break detection. Spontaneous behaviors and locomotor activity were automatically analyzed using EthoVision XT software (Noldus) over a continuous 24-hour period, encompassing both light and dark cycles. All analyses were conducted under standard housing conditions.

Elevated plus maze test

The elevated plus maze consisted of four arms, elevated 50 cm above the floor: two opposing open arms (30 × 5 cm, without walls) and two opposing closed arms (30 × 5 cm, enclosed by 15 cm high opaque walls). Mice were individually placed at the center of the maze, facing an open arm, and allowed to explore freely for 5 minutes. Behavior was recorded using a top-mounted video camera and analyzed with tracking software. The following parameters were quantified: time spent in open vs. closed arms, number of entries into open and closed arms (entry defined as all four paws entering an arm), and total distance traveled.

Light-dark box test

Mice were tested in a light-dark box apparatus consisting of two compartments: a brightly lit compartment (20 cm × 20 cm × 30 cm) and a dark compartment of identical size, connected by a small opening (7 cm × 7 cm) that allows free movement between the two chambers. Each mouse was gently placed in the center of the light compartment, facing away from the opening, and allowed to explore both compartments freely for a 5-minute session. Behavioral activity was recorded using an automated video tracking system. Parameters measured included the latency to the first transition from light to dark, the total time spent in the light compartment, and the number of transitions between the compartments.

QUANTIFICATION AND STATISTICAL ANALYSIS

For quantification of spine enrichment in Figures 3C and 5F, the enrichment fold was defined as the ratio of average fluorescent intensity in dendritic spine divided by the average fluorescent intensity in dendritic shaft. The background intensity was subtracted. The enrichment fold of 20-30 spines from one neuron was averaged as one data point.

For quantification of enrichment fold in Figure S4B, the enrichment fold was defined as the ratio of average fluorescent intensity in the droplet divided by the average fluorescent intensity in dilute phase (solution).

Please cite this article in press as: Jia et al., Shank3 oligomerization governs material properties of the postsynaptic density condensate and synaptic plasticity, Cell (2025), https://doi.org/10.1016/j.cell.2025.07.047

Statistical parameters including the definitions and exact values of n (e.g., number of experiments, number of spines, number of cells, etc.), distributions and deviations are reported in the figures and corresponding figure legends. Generally, data of *in vitro* phase separation assay are expressed as mean ± SD, and data of primary neuron culture, and electrophysiology are expressed as mean ± SEM, unless specified in the legends. n.s., not significant, *P < 0.05, **P < 0.01, ***P < 0.001, ****P < 0.0001 using student t-test or one-way ANOVA with Tukey's multiple comparison test. None of the data were removed from our statistical analysis as outliers. Statistical analysis was performed in GraphPad Prism. Experiments of neuronal culture imaging were performed in blind fashion, except for live cell-based experiments.

Supplemental figures

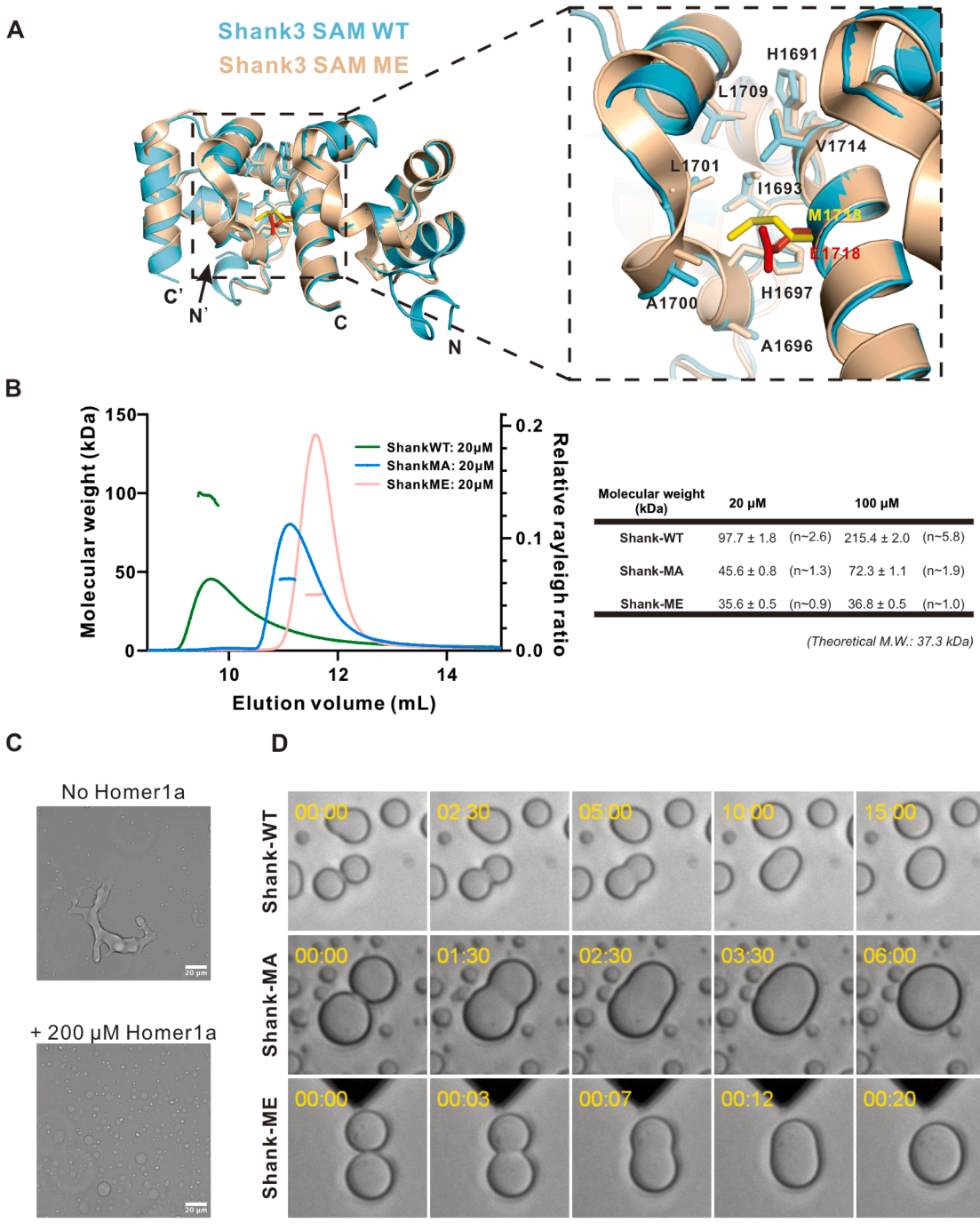

Figure S1. Decrease of Shank3 oligomerization softens the PSD condensate, related to Figure 1

(A) Direct alignment of two SAMs at one pair of head-to-tail surfaces. Shank3 SAM WT (PDB: 9KSQ) from this paper was labeled as cyan, and Shank3 SAM ME (PDB: 2F3N) from Baron et al.[56] was labeled as wheat. The zoomed-in view shows they share the same hydrophobic surface and involved the same other hydrophobic side chains.

(legend continued on next page)

(B) FPLC-coupled static light scattering showing the oligomerization states of recombinant Shank-WT, Shank-MA, and Shank-ME (20 μM). The fitted molecular weight is listed in the table showing the concentration-dependent oligomerization of Shank proteins and presented as mean ± SD.
(C) DIC images showing that 200 μM Homer1a dispersed the gel-like 4x PSD condensates (10 μM of PSD-95-PSG, GKAP, Shank-WT, and Homer individually, top panel) to soft liquid-like droplets (bottom panel). Scale bar, 5 μm.
(D) Time-lapse images showing the fusion process of 4x PSD condensate droplets containing Shank-WT, Shank-MA, or Shank-ME, respectively. Time is formatted as mm:ss. Note that the condensate droplets containing Shank-WT fused very slowly whereas droplets containing Shank-ME fused rapidly (20 min versus 30 s). Scale bar, 10 μm.

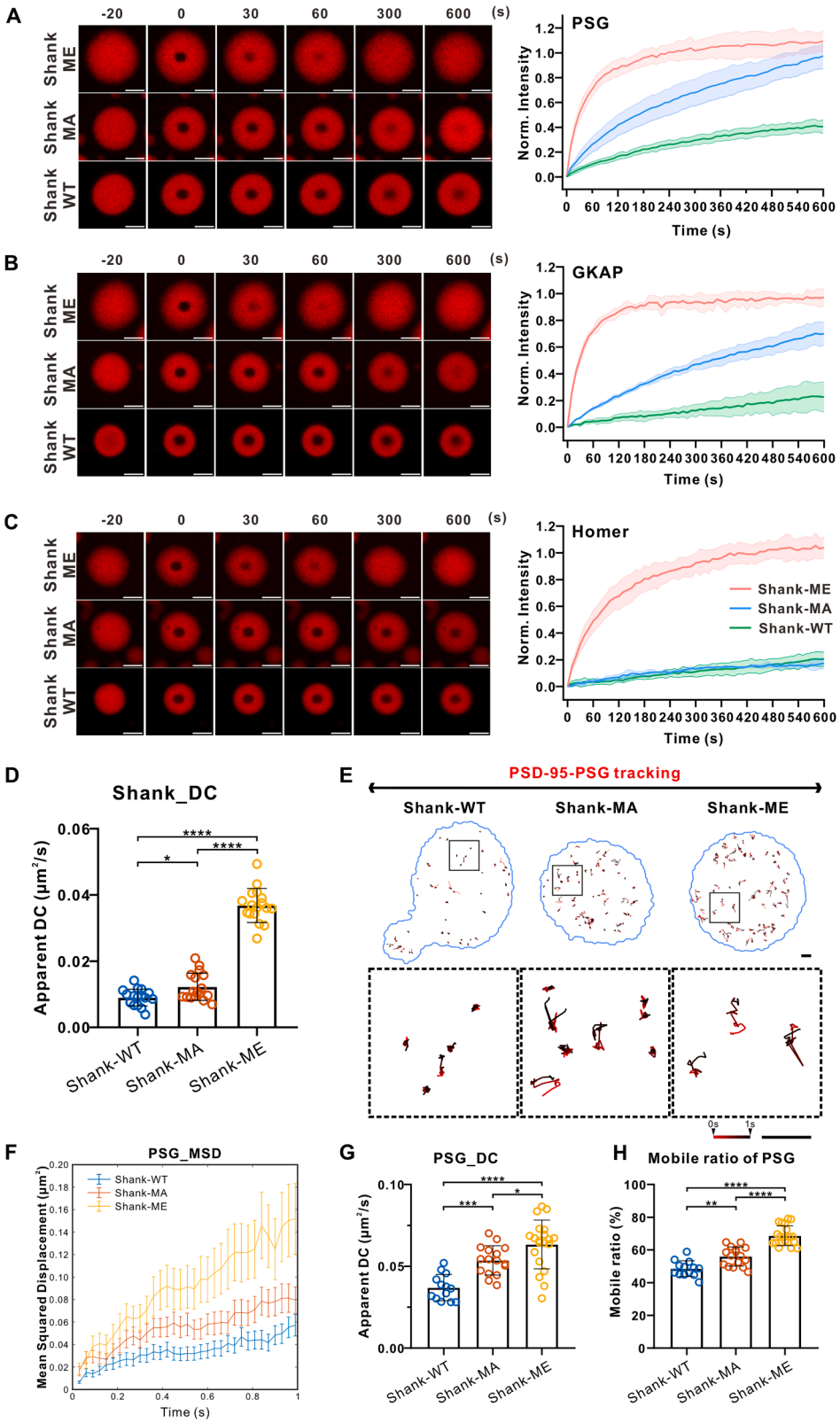

(legend on next page)

Figure S2. Dynamics of various PSD proteins in the 4x PSD condensates containing Shank-WT, Shank-MA, or Shank-ME, related to Figure 2

(A) Left panel: representative time-lapse images showing the fluorescence recovery of PSD-95-PSG molecules in 4x PSD condensates after photobleaching. Right panel: quantification of the FRAP experiments. Data were presented as mean ± SD. *n* = 12/12/9 droplets for Shank-WT/Shank-MA/Shank-ME, respectively. Protein concentration: 10 μM for each component. Scale bar, 5 μm.

(B) Left panel: representative time-lapse images showing the fluorescence recovery of GKAP molecules in 4x PSD condensates after photobleaching. Right panel: quantification of the FRAP experiment. Data were presented as mean ± SD. *n* = 3/4/3 droplets for Shank-WT/Shank-MA/Shank-ME, respectively. Protein concentration: 10 μM for each component. Scale bar, 5 μm.

(C) Left panel: representative time-lapse images showing the fluorescence recovery of Homer molecules in 4x PSD condensates after photobleaching. Right panel: quantification of the FRAP experiment. Data were presented as mean ± SD. *n* = 3/3/3 droplets for Shank-WT/Shank-MA/Shank-ME, respectively. Protein concentration: 10 μM for each component. Scale bar, 5 μm.

(D) Quantification of apparent diffusion coefficients of Shank molecules from Shank-WT, Shank-MA, and Shank-ME condensates using linear fitting of each MSD curve. Data were collected from three independent batches of experiments and shown as mean ± SD. *n* = 17/17/17 droplets for Shank-WT/Shank-MA/ and Shank-ME, respectively. One-way ANOVA followed by Tukey's post hoc test; $^{*}p < 0.05$, $^{****}p < 0.0001$.

(E) Representative images showing 1 s duration of the single molecule trajectories of PSD-95-PSG proteins within the condensates. Zoomed-in images are at the bottom panel. Red, t = 0; black, t = 1 s. Scale bar, 1 μm.

(F) MSD analysis of PSD-95-PSG tracks from condensates containing Shank-WT, Shank-MA, and Shank-ME, respectively. Data were collected from three independent batches of experiments and shown as mean ± SEM. *n* = 1,093/1,648/889 trajectories from 13/16/20 condensates for Shank-WT/Shank-MA/Shank-ME, respectively.

(G) Quantification of apparent diffusion coefficient of PSD-95-PSG in Shank-WT, Shank-MA, and Shank-ME containing 4x PSD condensates. Data were collected from three independent batches of experiments and shown as mean ± SD. *n* = 13/16/20 droplets for Shank-WT/Shank-MA/and Shank-ME, respectively. One-way ANOVA followed by Tukey's post hoc test; $^{*}p < 0.05$, $^{***}p < 0.001$, $^{****}p < 0.0001$.

(H) Quantification of the mobile ratio of PSD-95-PSG from Shank-WT, Shank-MA, and Shank-ME containing 4x PSD condensates. Data were collected from three independent batches of experiments and shown as mean ± SD. *n* = 13/16/20 droplets for Shank-WT/Shank-MA/and Shank-ME, respectively. One-way ANOVA followed by Tukey's post hoc test; $^{**}p < 0.01$, $^{****}p < 0.0001$.

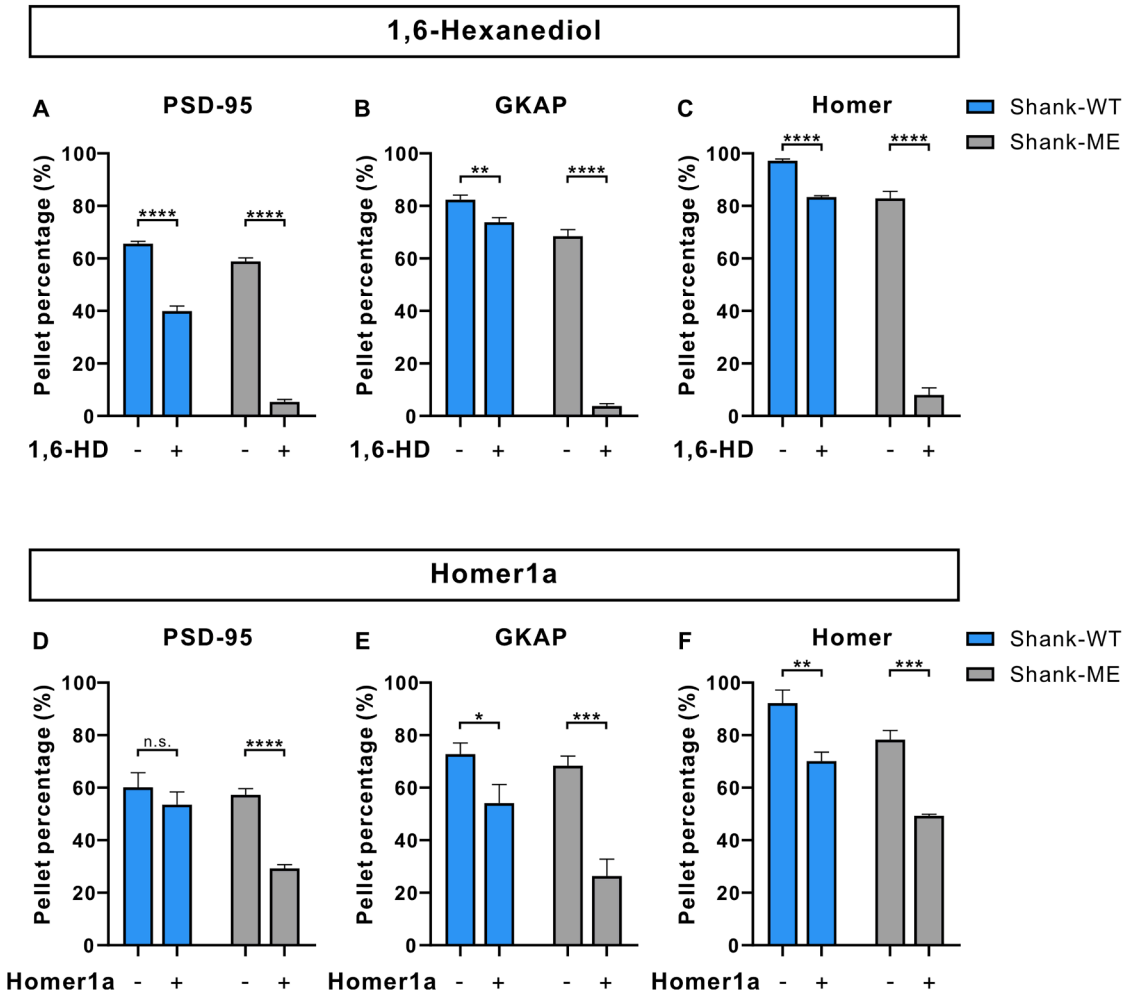

Figure S3. Resistance of the 4x PSD condensates containing Shank-WT, Shank-MA, or Shank-ME to condensate dispersion perturbations, related to Figure 2

(A–C) Quantification data showing the pellet percentage of PSD-95 (A), GKAP (B), and Homer (C) of the 1,6-hexanediol treatment assay in Figure 2J. Data were from 3 independent batches of sedimentation assay and presented as mean ± SD.

(D–F) Quantification data showing the pellet percentage of PSD-95 (D), GKAP (E), and Homer (F) of the Homer1a treatment assay in Figure 2L. Data were from 3 independent batches of sedimentation assay and presented as mean ± SD.

Unpaired t test; n.s., not significant; *$p < 0.05$, **$p < 0.01$, ***$p < 0.001$, ****$p < 0.0001$.

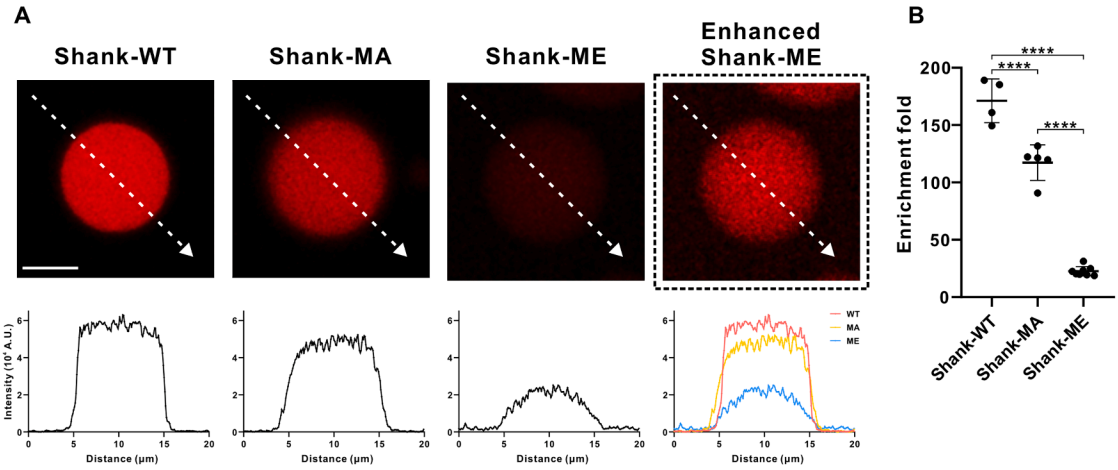

Figure S4. Enrichment of PSD-95 in the 4x PSD condensates containing Shank-WT, Shank-MA, or Shank-ME, related to Figure 3

(A) Line scanning analysis of the Cy3-PSD-95-PSG signal from the 4x PSD condensates containing Shank-WT, Shank-MA, or Shank-ME, respectively. Images were acquired from the same setting. In the dashed box, the signal of Shank-ME was further enhanced by adjusting the contrast of the image at left for easy visualization. Scale bar, 5 μm.

(B) Quantification of enrichment fold of PSD-95-PSG from the 4x PSD condensate containing Shank-WT, Shank-MA, or Shank-ME, respectively. Data were presented as mean ± SD. $n = 4/5/8$ droplets from the Shank-WT/Shank-MA/Shank-ME group. One-way ANOVA followed by Tukey's post hoc test; ****$p < 0.0001$.

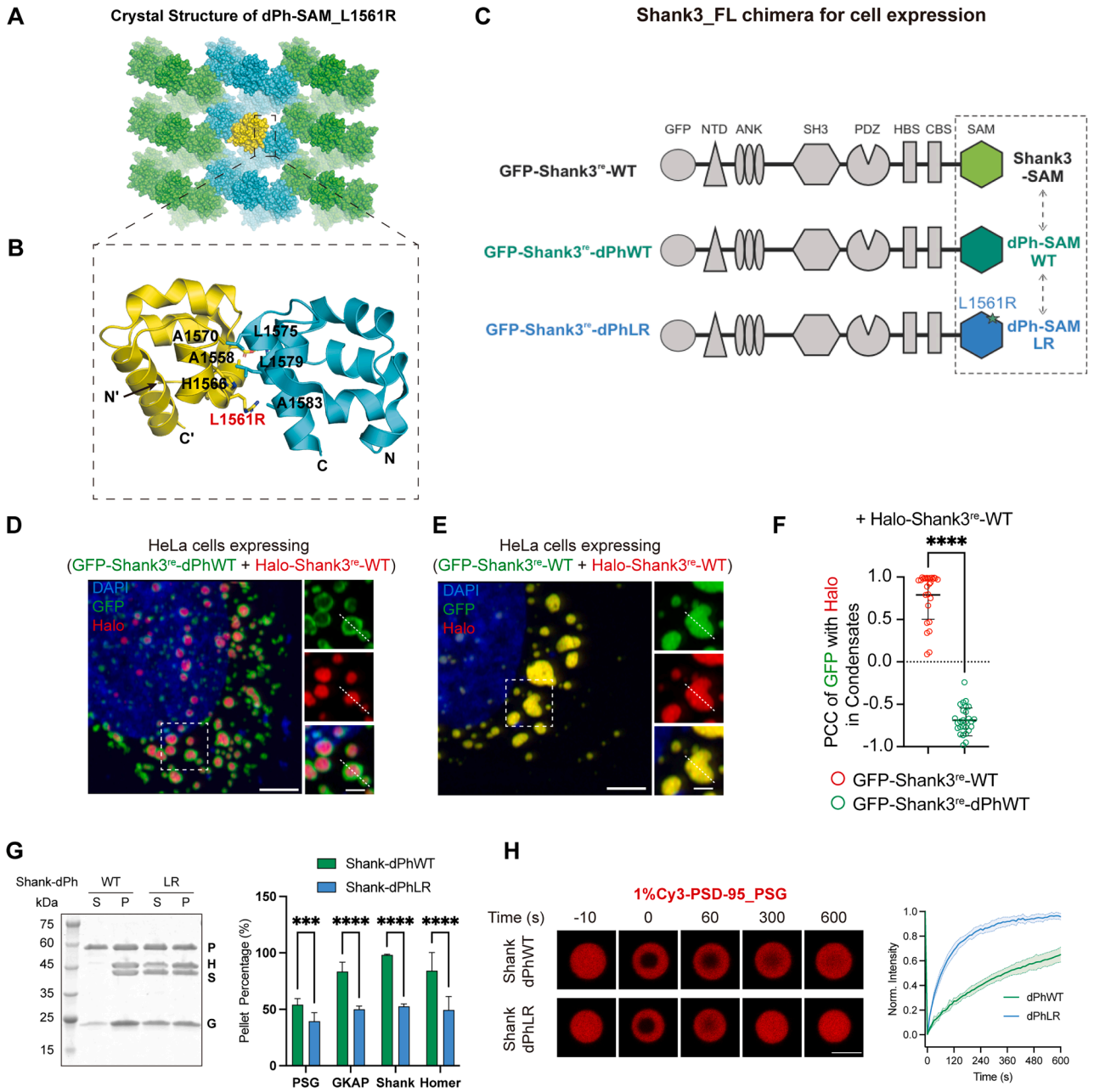

Figure S5. Design and validation of orthogonality, oligomerization, and phase separation of Shank-dPhSAM, related to Figure 5

(A) Crystal packing representation of the Drosophila polyhomeotic SAM domain (dPh-SAM) monomeric mutant (L1561R, from PDB: 1kw4)[74] showing the helical fiber-mediated sheet formation.

(B) Zoomed-in image illustrates that L1561R is located at the center of the hydrophobic interface between two SAM domains forming each individual fiber.

(C) Schematic diagram showing the design of GFP-Shank3^{re}-dPhSAM chimera proteins used in cell-based assays.

(D) Left panel: representative fluorescence images of cells showing demixed cellular puncta enriched either GFP-Shank3^{re}-dPhWT (green) or Halo-Shank3^{re}-WT (red). Right panel shows the zoomed-in view of regions marked by dashed squares. Scale bar, 5 and 1 μm for zoomed-in views.

(E) Left panel: representative fluorescence images of cells showing mixed cellular puncta enriched both GFP-Shank3^{re}-WT (green) and Halo-Shank3^{re}-WT (red). Right panel shows the zoomed-in view of regions marked by dashed squares. Scale bar, 5 and 1 μm for zoomed-in views.

(F) Quantification of GFP-Shank3^{re}-dPhWT or GFP-Shank3^{re}-WT and Halo-Shank3 ^{re}-WT puncta demixing by plotting Pearson correlation coefficient (PCC) values. Data were collected from two independent batches. n = 27 cells. Error bars indicate ± SD. Unpaired t test; ****$p < 0.0001$.

(G) Left panel: representative SDS-PAGE showing the fraction distributions of the four PSD proteins recovered in the dilute phase/supernatant (S) and in the condensed phase/pellet (P). The concentration was 5 μM for each component. For the protein band labeling, P, PSD-95-PSG supramodule; H, Homer; S, Shank; G, GKAP. Right panel: quantification data showing the pellet percentage from left panel. Data were from 6 independent batches of sedimentation assays and presented as mean ± SD. Unpaired t test; ***$p < 0.001$, ****$p < 0.0001$.

(legend continued on next page)

(H) Left panel: representative time-lapse images showing the fluorescence recovery of PSD-95_PSG molecules in the 4x PSD condensates after photobleaching. The concentration of each protein was 10 μM. PSG molecules were labeled with Cy3 at a ratio of 1%. Scale bar, 5 μm. Right panel: quantification analysis of FRAP experiments. Data were collected from two independent batches of condensates for each Shank-dPh variant and presented as mean ± SD. *n* = 10 droplets.

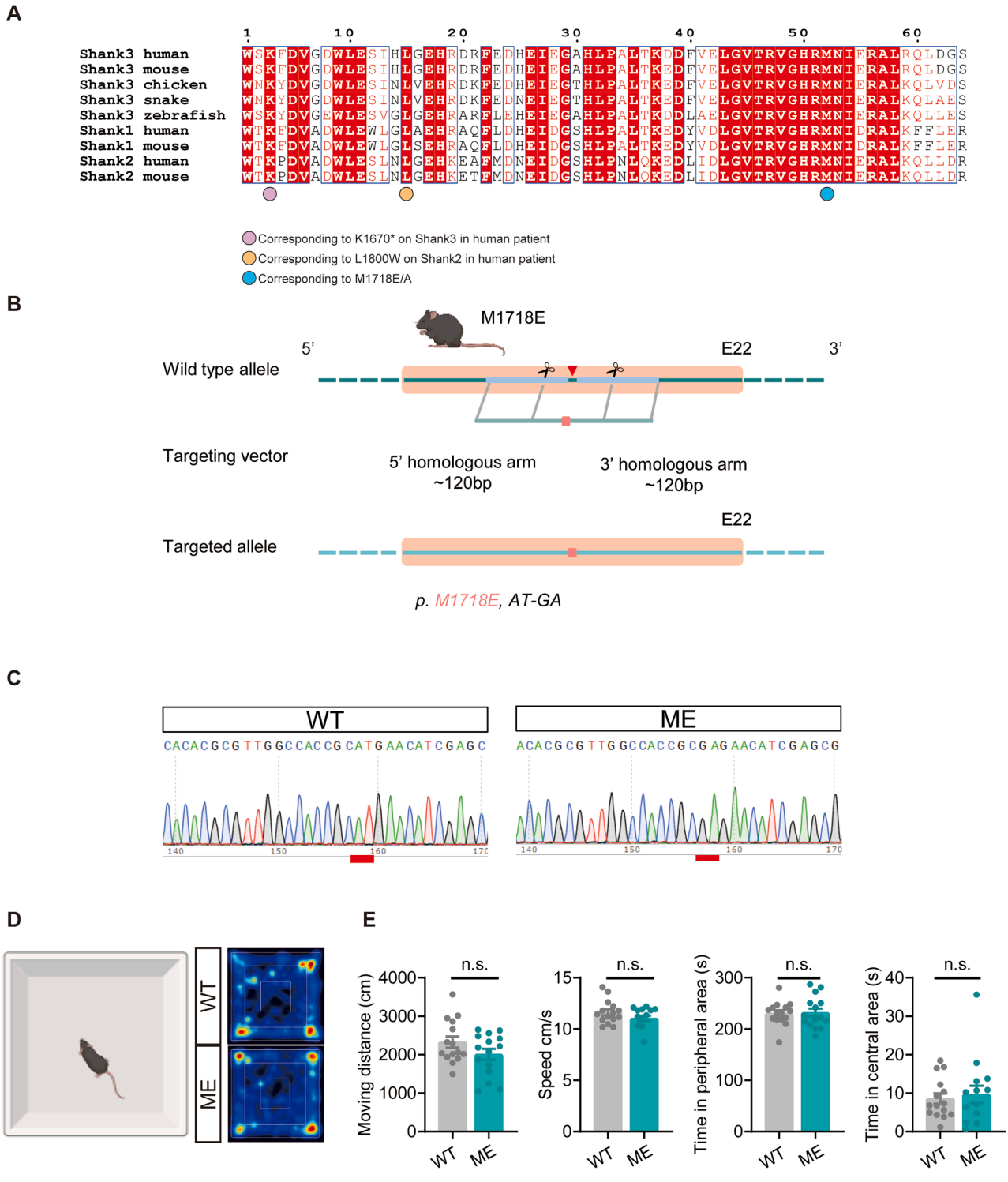

Figure S6. The conservation analysis of SAM domains of the Shank family proteins and generation of *Shank3*^{M1718E} mice, related to Figure 7

(A) Sequence alignment of the Shank SAM domains in vertebrates. Sequence alignment showing the conservation of the Shank SAM domain. The K1670* mutation in human Shank3, the missense mutation L1800W in human Shank2, and the designed M1718E/A in mouse Shank3 are indicated by purple, yellow, and blue circles, respectively. The access numbers for the proteins are Shank1 human, Uniprot: Q9Y566; Shank1 mouse, Uniprot: D3YZU1; Shank2 human, Uniprot: Q9UPX8; Shank2 mouse, Uniprot: Q80Z38; Shank3 human, Uniprot: Q9BYB0; Shank3 mouse, Uniprot: Q4ACU6; Shank3 chicken, NCBI: XP_025008646.2; Shank3 snake, NCBI: XP_032077574.1; and Shank3 zebrafish, NCBI: XP_009298459.1.

(legend continued on next page)

(B) Schematic strategies for generating *Shank3*^{M1718E} mutant mice using CRISPR-Cas9. gRNA recognition sites are indicated with scissors. The targeting vector includes homologous arms (~120 bp each) flanking the M1718E mutation site, leading to the substitution of AT with GA.
(C) Sequencing analysis showing the WT and *Shank3*^{M1718E} mutant alleles. The homozygous *Shank3*^{M1718E} mutant allele contains the M1718E substitution, as indicated by the red box highlighting the base pair change.
(D) Representative heatmaps of movement trajectories for WT male and homozygous *Shank3*^{M1718E} mutant (ME) male mice in the open field test.
(E) Quantification of open field parameters, including total moving distance (cm), average speed (cm/s), time spent in the peripheral area (s), and time spent in the central area (s). Data were presented as individual values with mean ± SEM (n = 15 mice; unpaired t test; n.s., not significant).

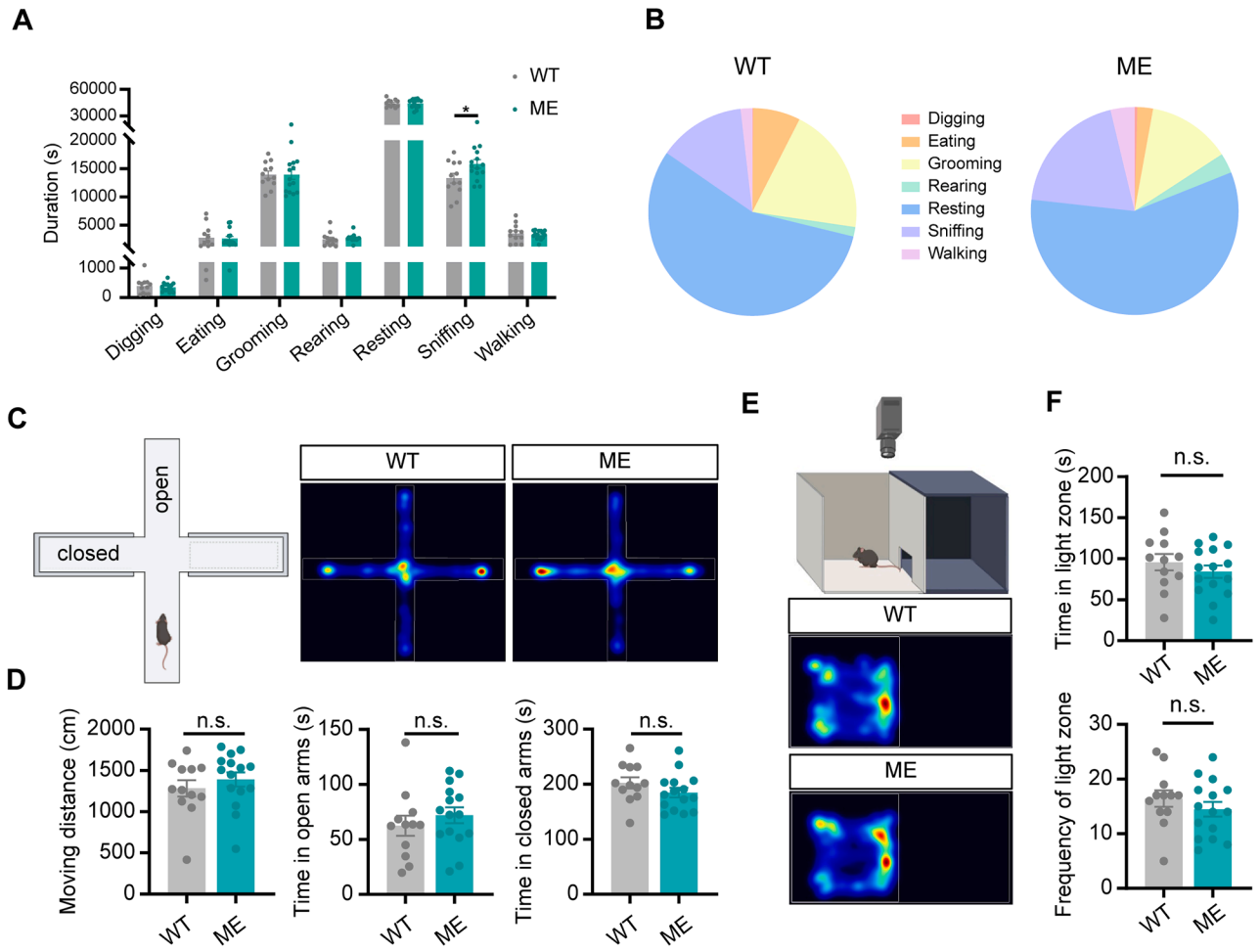

Figure S7. The Shank3^{M1718E} mice exhibit no significant anxiety-like behavioral phenotype, related to Figure 7

(A) Bar graph showing 24-h natural spontaneous behaviors. Data are presented as mean ± SEM (n = 12–15 mice; unpaired t test; *p < 0.05).

(B) Pie chart summary showing the 24-h natural spontaneous behaviors.

(C) Schematic representation of the elevated plus maze (EPM) test and representative heatmaps of movement trajectories in the test.

(D) Bar graph showing the time spent in the open and closed arms of the EPM. Data were presented as mean ± SEM (n = 12–15 mice per group; ns, not significant; unpaired t test).

(E) Schematic of the light-dark box test and representative movement heatmaps.

(F) Bar graph showing the time spent in the light zone (top) and frequency of entries into the light zone (bottom). Data were shown as mean ± SEM (n = 12–15 mice per group; n.s., not significant; unpaired t test).